Interferon Epsilon Protects Epithelial Barriers from Viral Infection through Autocrine Intracellular Signaling

Rebecca L. Casazza[1], Samantha Skavicus[2], David Hare[1], Kaila A. Cooley[1], Nicholas S. Heaton[2,3], Carolyn B. Coyne[1,3]

1) Duke University School of Medicine, Department of Integrative Immunobiology, Durham, NC
2) Duke University School of Medicine, Department of Microbiology and Molecular Genetics, Durham, NC
3) Duke Human Vaccine Institute, Durham, NC

*Address correspondence:
Carolyn Coyne, PhD
3130 Medical Sciences Research Building III
3 Genome Court
Durham, NC 27710
USA
carolyn.coyne@duke.edu

Abstract

Antiviral defenses at mucosal barriers are essential for preventing viral entry and systemic infection. Interferon epsilon (IFNε), a unique type I interferon not induced by infection, is constitutively expressed in the female reproductive tract (FRT), where it provides broad antiviral protection and fluctuates with hormone status. The role of IFNε outside the FRT remains unclear, although it is expressed in the intestinal epithelium. We generated an IFNε knockout mouse (*Ifnε-/-*) and confirmed its antiviral activity in the FRT. Using single-cell RNA sequencing of the cycling mouse FRT, we show that *Ifnε* expression is restricted to specific epithelial cells, is not hormonally regulated, and induces basal interferon-stimulated genes in an autocrine manner. scRNASeq of WT and *Ifnε*$^{-/-}$ uteruses showed that loss of *Ifnε* reduced basal ISG levels in *Ifnε*-expressing epithelial cells without impacting other cell types. Consistent with this, IFNε was retained intracellularly in primary human FRT cells. scRNASeq of human stem cell-derived enteroids and tissue revealed that multiple GI epithelial cells express high basal IFNε levels, and *Ifnε-/-* mice are more susceptible to enteric viral infection. Our findings reveal that IFNε is an intracellular IFN that provides mucosal immunity across various epithelial tissues, extending its protective functions beyond the FRT.

Introduction

Antiviral defenses at barrier sites are essential for preventing entry and dissemination of viruses, which could compromise tissue integrity and lead to systemic infection. In the reproductive tract, these defenses are particularly crucial given exposure to external pathogens, such as sexually transmitted viruses, and their essential role in safeguarding reproductive health and ensuring successful reproduction. Robust antiviral responses are essential for maintaining a balanced immune environment within the reproductive tissue niche, minimizing the risk of infection while preserving tissue function and integrity.

Interferon epsilon (IFNε) is a type I IFN that has been described as specifically enriched in the epithelial cells of the female reproductive tract (FRT) (Bourke et al., 2022; Fung et al., 2013). Unlike other type I IFNs, IFNε is constitutively expressed and is not induced by viral infections. Despite its lack of induction by infection, IFNε plays a direct role in innate antimicrobial defense against sexually transmitted infections, including HIV, herpes simplex virus (HSV), Zika virus (ZIKV), and Chlamydia (Coldbeck-Shackley et al., 2023; Fung et al., 2013; Stifter et al., 2018). In addition to its role in antiviral defenses, IFNε may also play a direct role in tumorigenesis in the FRT, where it exerts tumor suppressive activities in the epithelial cells of the fallopian tubes (Marks et al., 2023).

IFNε has also been proposed to play a role in pregnancy, as it is expressed in the human myometrium, cervix, and chorioamniotic membranes, suggesting a constitutive role in host defense mechanisms at these sites (Miller et al., 2022). It is also elevated in amniotic fluid during spontaneous preterm labor with intra-amniotic infection (Miller et al., 2022), indicating a potential role in antimicrobial responses within the amniotic cavity. However, consistent with viral infections, its expression is not enhanced by bacterial stimulation *in vitro*, suggesting alternative sources of IFNε during infection (Fung et al., 2013; Miller et al., 2022).

Several clues exist as to the regulation of *IFNε* expression. Analysis of the *IFNε* promoter region revealed progesterone response elements implicating hormonal modulation in its

expression (Hardy et al., 2004). Consistent with this, *Ifnε* expression fluctuates in the mouse uterus with the estrous cycle, and peaks during estrous when progesterone levels are highest (Fung et al., 2013). The transcription factor ELF3, which directly regulates the expression of genes important for maintaining the integrity and function of epithelial barriers, contributes to the control of IFNε expression in the uterus and levels fluctuate with estrous status (Fung et al., 2024). Transcription factor binding site analysis has also revealed potential regulatory sites for NF-κB, a critical mediator in immune and inflammatory responses (Hardy et al., 2004). NF-κB binding elements in the IFNε promoter suggest that this cytokine might be responsive not only to hormonal signals but also to cellular stress and inflammatory stimuli, which aligns with its role in epithelial immune defense. Indeed, treatment of cells with tumor necrosis factor-α (TNF-α) upregulates *IFNε* expression (Matsumiya et al., 2007). Taken together, these findings suggest that *IFNε* expression may be finely tuned by both hormonal and inflammatory cues, with transcription factors including NF-κB and ELF3 potentially coordinating epithelial immune readiness in response to estrous phase and/or local environmental stimuli.

In addition to antimicrobial and antitumor properties in the epithelium of the FRT, IFNε potentially plays a role in modulating the immune system. For example, *Ifnε*$^{-/-}$ mice exhibit less uterine NK cell accumulation at baseline and less activation after infection than WT mice, a phenotype which results in part from differences in cytokine secretion in *Ifnε*$^{-/-}$ macrophages/monocytes (Mayall et al., 2024). Additionally, T-, B-, and NK cells respond to recombinant IFNε *in vitro* (Stifter et al., 2018). These findings suggest that IFNε not only fortifies epithelial defenses but also plays a broader immunoregulatory role in the FRT, coordinating both innate and adaptive immune responses to maintain tissue homeostasis and readiness against infection.

Recent studies have suggested that IFNε might also play a role in inflammatory signaling outside of the FRT. In addition to epithelial cells of the FRT, *Ifnε* is expressed in the intestinal

52 epithelium, where it helps limit inflammation and supports the intestinal regulatory T cell
53 compartment (de Geus et al., 2024). In rhesus macaques, IFNε is expressed in the epithelium of
54 the large and small intestines, lung, and foreskin in addition to the female reproductive tract
55 (Demers et al., 2014). These studies highlight IFNε as a multifaceted cytokine with roles in
56 maintaining immune balance across diverse mucosal tissues, suggesting it may provide a
57 widespread defense mechanism beyond the FRT.

58 The mechanisms underlying the regulation of IFNε and its effects on antiviral responses
59 beyond the FRT are incompletely defined. In this study, we generated an IFNε knockout mouse
60 model (*Ifnε*$^{-/-}$) using a modified intracytoplasmic gene editing via oviductal nucleic acids delivery
61 (iGONAD) technique, which allows for *in vivo* genetic modifications without the need for embryo
62 transfer (Ohtsuka et al., 2018; Skavicus and Heaton, 2023). We confirmed that, like a previously
63 described *Ifnε*$^{-/-}$ mouse model (Fung et al., 2013), IFNε exerts antiviral activity against intravaginal
64 infection with herpes simplex virus-2 (HSV-2) in this model. Analysis of single-cell RNA
65 sequencing (scRNA-Seq) datasets across the estrous cycle in the mouse FRT (Winkler et al.,
66 2024) revealed that *Ifnε* is expressed in tissue-specific epithelial cell clusters and is not directly
67 regulated by the estrous cycle. However, its expression varies due to fluctuations in the
68 populations of *Ifnε*-expressing epithelial cells throughout the cycle. We also found that *Ifnε*-
69 expressing epithelial populations expressed high levels of interferon-stimulated genes (ISGs),
70 which were absent in epithelial cell types lacking *Ifnε* expression, suggesting an autocrine role for
71 IFNε. Consistent with this, scRNA-Seq analysis of uterine tissues from WT and *Ifnε*$^{-/-}$ mice
72 showed that deletion of *Ifnε* significantly reduced interferon stimulated gene (ISG) expression in
73 specific epithelial cell populations, without affecting other transcripts. In human primary FRT cells,
74 we found that IFNε was constitutively expressed, not induced by pathogens, and remained non-
75 secreted. Additionally, using scRNASeq of human stem cell derived enteroids and analysis of
76 existing human tissue datasets, we found that IFNε is constitutively expressed in several cell types
77 in the human intestine (e.g., mature enterocytes, Tuft cells) and exerts antiviral activity against

the enterovirus coxsackievirus B (CVB) in the intestine *in vivo*. These findings highlight IFNε as an important contributor to mucosal immunity, supporting antiviral defenses in tissue-specific epithelial cells across the FRT and intestine and expand our understanding of its role beyond traditional pathogen-induced responses.

Results

Generation of *Ifnε*$^{-/-}$ mice using iGONAD

We used a modified iGONAD protocol (Skavicus and Heaton, 2023) to generate an *Ifnε*$^{-/-}$ knockout mouse. The iGONAD technique was chosen for its efficiency and precision in gene editing, particularly in the context of creating knockout models. To achieve this, we employed a dual sgRNA approach targeting the single coding exon of the *Ifnε* gene, which resulted in a 263 basepair deletion (**Figure 1A, Supplemental Figure 1A**). 15 total pups were born following the injection and electroporation of sgRNAs and Cas9 into the oviducts of pregnant dams,. These pups were subsequently screened for *Ifnε* knockout by PCR using primers spanning both gRNA target sites. The genotyping results revealed that 6 out of the 15 pups were homozygous for the *Ifnε* deletion, indicating a successful knockout of both alleles. Additionally, 3 pups were identified as heterozygous, carrying one wildtype and one knockout allele, while the remaining 6 pups were wildtype (representative genotypes, **Figure 1B**). Successful gene knockout was further validated by Sanger sequencing, which confirmed the deletion at the nucleotide level (**Figure Supplemental 1B**). Following this, a qPCR-based genotyping assay was developed in collaboration with a commercial vendor (Transnetyx) to streamline the genotyping process for subsequent generations. To establish a stable knockout line one animal (15) identified as homozygous for the *Ifnε* deletion was selected as the founding sire. To ensure genetic integrity and minimize potential off-target effects, this animal was backcrossed ~6 times with C57Bl/6J mice. Following backcrossing, a stable and reproducible *Ifnε*$^{-/-}$ line was developed and used for subsequent studies.

104 To confirm that this newly established *Ifnε*$^{-/-}$ line recapitulated phenotypes observed in a
105 previous *in vivo* model (Fung et al., 2013) regarding the role of IFNε in antiviral signaling in the
106 FRT, we infected *Ifnε*$^{-/-}$ and WT female mice intravaginally with 100PFU of HSV-2 (strain 333) and
107 scored mice daily for clinical signs. Despite equivalent weight loss (**Figure 1C**), a higher
108 percentage of *Ifnε*$^{-/-}$ mice had disease onset compared to WT mice (77% vs 40%), defined as any
109 observable clinical sign, (**Figure 1D**) and a higher percentage of *Ifnε*$^{-/-}$ mice succumbed to
110 infection (70% vs 46%) (**Figure 1E**). Disease peaked at ~10dpi and *Ifnε*$^{-/-}$ mice displayed higher
111 frequencies of advanced clinical signs throughout the course of infection (**Figure 1F**). Following
112 infection with 10,000PFU of HSV-2, *Ifnε*$^{-/-}$ had higher viral burdens in vaginal lavages at 2 and 3dpi
113 (**Figure 1G**) and had significantly worse clinical outcomes measured by clinical scores (**Figure**
114 **1H**). Taken together, these data show that *Ifnε*$^{-/-}$ mice generated using iGONAD recapitulate the
115 heightened susceptibility and impaired antiviral response observed in a previous *in vivo* model of
116 HSV-2 infection in the FRT.
117

118 ***Ifnε* is expressed in epithelial cells of the oviduct, uterus, cervix, and vagina independent**
119 **of estrous status**

120 To determine the specific cell types expressing *IFNε* in the FRT, and to determine the
121 impact of the estrous cycle on this expression, we analyzed an existing single cell atlas of the
122 cycling mouse female reproductive tract based on 378,516 cells from normal cycling young mice
123 in the four cycle phases (proestrus [Pro], estrus [Est], metestrus [Met], and diestrus [Di]) (Winkler
124 et al., 2024). The dataset contained cells harvested from ovary, oviduct, uterus, cervix, and vagina
125 from 3-5 independent animals. We restricted our analyses to non-pregnant young mice (aged <12
126 months). A total of 71173 (Ovary), 75091 (Oviduct), 49889 (Uterus), 78967 (Cervix), and 82861
127 (Vagina) cells passed quality control and were used for cluster analysis and cell-type specific
128 marker expression analysis following integration to correct for batch effects (**Figure 2A, Figure**
129 **S2A-J**). We broadly clustered cells into epithelial cells (EpC), stromal cells, immune cells,

endothelial cells (EndoC), or muscle cells. Each tissue site exhibited site-specific enrichment of these cell types, consistent with what has been described (Winkler et al., 2024), with the cervix and vagina most enriched in EpCs and ovary, oviduct, and uterus more enriched in stromal cells (**Figure 2A**, **Figure S2A-J**). While there was slight variation in the proportion of these cell types during the estrous cycle, including the enrichment of immune cell types in the cervix and vagina during Met, the proportion of cell types were largely maintained across all tissues (**Figure 2B**).

We next determined the cell type(s) expressing *Ifnε* across all tissue sites and defined the impact of the estrous cycle on this expression. For this analysis, we further clustered cell types to increase resolution. In the oviduct, uterus, cervix, and vagina, we found that *Ifnε* was specifically enriched in EpC cell types that also expressed high levels of epithelial markers (e.g., *Cdh1*, *EpCam*) (**Figure 2C**). We did not detect any *Ifnε* in the ovaries (**Figure 2C**). We next determined the levels of *Ifnε* expressed in EpCs across the estrous cycle in all tissues. In the oviduct, cervix, and vagina, we observed highly similar levels of expression across all stages of the estrous cycle (**Figure 2D**). In the uterus, levels of *Ifnε* were consistent across Pro, Est, and Di, with significantly lower levels in Met (**Figure 2D**). Similarly, *Ifnε* levels were low in the uterus of pregnant mice (**Figure S2K, S2L**). Taken together, these data indicate that IFNε is predominantly expressed in epithelial cell types across the FRT, with consistent expression levels across the estrous cycle, except in the uterus where levels significantly decrease during Met and pregnancy.

***Ifnε*-expressing epithelial cells in the FRT express high basal ISGs**

The FRT is lined by specialized epithelial cell types, each with distinct functions tailored to their anatomical location. These include ciliated and secretory EpCs in the oviduct, luminal and glandular EpCs in the uterus, mucus-secreting EpCs in the cervix, and stratified squamous EpCs in the vagina. Given that *Ifnε* was expressed in EpC populations across the FRT, we next sought to identify the specific EpC populations responsible for this expression and whether it varied by location. Furthermore, we sought to investigate whether *Ifnε*-expressing epithelial cell populations

156 exhibited distinct transcriptional profiles, including elevated ISG levels. To do this, we subsetted
157 the EpC cell cluster from all anatomical sites and re-clustered to obtain better resolution between
158 distinct EpC types. In the oviduct, EpC cells were clustered into ciliated (cEpC) and secretory
159 (SEpC) populations, which were distinguished based upon marker expression (**Figure 3A-3B**).
160 We found that *Ifnε* was specifically expressed in an SEpC cell population marked by *Serpina1e*
161 expression (**Figure 3C, 3D**). This population also exhibited high basal levels of ISGs (**Figure 3C**).
162 In the uterus, EpCs were distinguished between markers associated with luminal EpCs (LEpCs)
163 and glandular EpCs (GlEpCs) (**Figure 3E**), with *Ifnε* expression restricted to a LEpC population
164 expressing high levels of Tactstd2 (**Figure 3F-3H**). This cluster also expressed high levels of
165 diverse ISGs (**Figure 3G**). The cervix contained the largest number of EpCs, which sub-clustered
166 into intermediate (IEpCs), superficial (SuEpCs), and basal EpCs (BEpC), some of which were
167 proliferating (pBEpC) (**Figure 3I, 3J**). *Ifnε* was expressed in both SuEpC populations, with
168 significantly higher levels in the Sprr2d^{+} cluster, which also showed elevated ISG expression
169 (**Figure 3K, 3L**). The vaginal EpCs clustered into SuEpCs, BEpCs, and columnar EpCs
170 (ColEpCs), with ColEpCs expressing both *Ifnε* and basal ISGs (**Figure 3M-3P**). These data
171 demonstrate that *Ifnε* is expressed in specific epithelial cell populations across tissue sites, with
172 its expression correlating with high basal levels of ISG expression within these clusters.

173 The data described above suggested that *Ifnε* is expressed in distinct EpC types in an
174 anatomical location-specific manner, suggesting that these cell types might exhibit conserved
175 expression of factors responsible for *Ifnε* expression. To determine if this was the case, we
176 compared the differentially enriched genes in all *Ifnε* expressing clusters across anatomical sites
177 and identified the genes shared between these cell types. This analysis revelated that only 31
178 genes (1% of the total genes) were shared between *Ifnε* expressing EpC types (**Supplemental**
179 **Figure 3A**). The top-most gene shared across all cell clusters was *Elf3* (**Supplemental Figure**
180 **3B**), which has been shown previously to regulate *Ifnε* expression (Fung et al., 2024). In fact,
181 there were only two transcription factors shared between all *Ifnε*-expressing EpC clusters, which

182 included *Elf3* and *Maff* (**Supplemental Figure 3C**). These findings suggest that, despite the
183 anatomical specificity of *Ifnε* expression, only a small set of conserved transcription factors, which
184 included *Elf3*, may play a role in regulating *Ifnε* expression across diverse epithelial cell types.
185

186 **IFNε is a Key Modulator of Basal ISG Expression in the FRT Epithelium**

187 We observed high basal ISG expression exclusively in EpC clusters that also expressed *Ifnε*
188 across the FRT. To determine whether *Ifnε* expression was required for these basal levels, we
189 performed scRNASeq on uterine tissue isolated from WT and *Ifnε*$^{-/-}$ mice in estrous, with 19227
190 cells passing quality control. Cluster analysis and cell-type specific marker expression following
191 integration to correct for batch effects across independent animals revealed four distinct clusters
192 of EpCs, two populations of endothelial cells (Endo), stroma and fibroblasts, two populations of
193 muscle cells (Musc-1 and Musc-2), pericytes (Peri), and various immune cells including
194 macrophages (Mac), dendritic cells (DC), and NK cells (NK) (**Figure 4A**). There were near-
195 equivalent ratios of all cell types between WT and *Ifnε*$^{-/-}$ mice (**Figure 4B, Supplemental Figure**
196 **4A**) and cell clusters expressed cell type-specific markers, which were conserved between WT
197 and *Ifnε*$^{-/-}$ mice (**Figure 4C**, **Supplemental Figure 4B**). Consistent with the findings discussed
198 above, we identified a single cluster of EpCs (EpC-2) that highly expressed *Ifnε* and expressed
199 high basal ISG levels (**Figure 4D**). This cluster also expressed markers associated with LEpCs
200 (e.g., *Prap1*, *Tacstd2*, *Ltf*) (**Supplemental Figure 4C**, **4D**).

201 To assess whether *Ifnε* expression was required for basal ISG expression in EpC-2 and
202 other cell types, we performed pseudobulk differential expression analysis across all cell clusters
203 in WT and *Ifnε*$^{-/-}$ mice. We identified a total of 115 differentially downregulated transcripts in
204 *Ifnε*$^{-/-}$ mice compared to WT, with ~70% of these differentially expressed genes (DEGs) attributed
205 specifically to the EpC-2 cluster (**Supplemental Figure 4E**). Pathway analysis of these DEGs
206 showed a significant enrichment in genes associated with IFN signaling and the antiviral response
207 (**Figure 4E**). Of the 81 differentially downregulated DEGs in EpC-2, ~45% of them were ISGs

208 (**Figure 4F).** Several additional clusters also exhibited a downregulation of select ISGs (EpC-3,
209 EpC-4, Stroma, and DC), but the total number of DEGs was significantly lower than that observed
210 in EpC-2 (**Figure 4F**). Additional clusters, including EpC-1, Endo-2, Fib, and Musc-1 did not
211 exhibit any changes in gene expression in *Ifnε*$^{-/-}$ mice (**Figure 4F**). There were only two DEGs
212 enriched in *Ifnε*$^{-/-}$ mice, *Ppbp* and *Crct.* Importantly, although ISGs were significantly
213 downregulated in EpC-2, other non-IFN-mediated inflammatory transcripts were unchanged,
214 including those associated with IL1 signaling (e.g., *Il1a*), chemokine signaling (e.g., *Cx3cl1*), and
215 cytokine signaling (e.g., *Mif*) (**Figure 4G-4I**). Taken together, these data show that *Ifnε* expression
216 is crucial for maintaining basal ISG expression in EpC populations in the FRT.
217

218 **IFNε is retained intracellularly and is not induced by viral infections in primary human**
219 **epithelial cells**

220 To assess whether IFNε expression levels changed following infection, we cultured human
221 primary endometrial and vaginal epithelial cells, infected them with Sendai virus (SeV) or HSV-2,
222 or treated them with a variety of PAMPs including poly(I:C), cGAMP, and LPS, and measured
223 *IFNε* expression by qRT-PCR. Consistent with what we observed in the mouse scRNAseq
224 analysis described above, *IFNε* was basally expressed in both uterine and vaginal primary cells
225 and expression levels were unchanged with infection or PAMP treatment (**Figure 5A, 5B)**. In
226 contrast, *IFNβ* was undetected at baseline, and was induced by all conditions except for LPS
227 treatment (**Figure 5A, 5B).** To broadly profile the induction of *IFNε* and other IFNs, we performed
228 whole transcriptome bulk RNA-Seq on uterine and vaginal epithelial cells infected with SeV, as
229 well as on mock-infected controls. Both cell types responded to infection by induction of various
230 IFNs, including *IFNβ* and *IFNλ* 1-3, as well as canonical ISGs (e.g., *OAS1*, *OASL*, *ISG15*) (**Figure**
231 **5C-5E**). In contrast, although *IFNε* was expressed basally, it was not induced by SeV infection in
232 either cell type (**Figure 5D**, **5E**).

233 In our scRNAseq datasets, we observed basal ISG expression in clusters that also
234 expressed *Ifnε*, suggesting an autocrine role for IFNε signaling in subsets of epithelial cells of the
235 FRT. To determine if IFNε is retained intracellularly, we examined both lysates and supernatants
236 from human uterine and vaginal primary epithelial cells for IFNε or IFN-β levels by ELISA. IFNε
237 was undetectable in the supernatants from vaginal and uterine primary cells basally, after poly(I:C)
238 treatment, and after SeV infection (**Figure 5F, 5G**). However, there were high levels of IFNε
239 detected in the cell lysates in all conditions, although there was significantly more IFN-ε at
240 baseline than there was following poly(I:C) treatment or infection (**Figure 5F, 5G).** In contrast,
241 IFN-β was undetectable at baseline and although it could be observed at low levels in cell lysates
242 following poly(I:C) treatment or SeV infection, it was significantly higher in the supernatants
243 **(Figure 5H, 5I).** Together, these data indicate that IFNε is constitutively expressed and retained
244 intracellularly within epithelial cells of the FRT, where it likely functions through autocrine signaling,
245 in contrast to IFN-β, which is secreted in response to infection.
246

247 **IFNε is basally expressed in the gastrointestinal tract and protects against enteric virus**
248 **infection**

249 IFNε has been reported to be expressed in the gastrointestinal tract and may be associated with
250 colitis (de Geus et al., 2024). However, whether IFNε is expressed in select EpC subtypes in the
251 GI tract like the FRT or whether it exerts antiviral activity in the GI tract is unknown. To define the
252 expression of IFNε in the GI tract, we first generated human stem-cell derived enteroids and
253 performed scRNASeq. To include diverse GI cell types, human enteroids were grown in expansion
254 media (Exp) to maintain a proliferative state with stem and progenitor cells or under differentiation
255 conditions (Dif) to promote their maturation into specialized cells, including enterocytes, goblet
256 cells, and Paneth cells (Fujii et al., 2018; He et al., 2022). Enteroids cultured under these
257 conditions contained $CD24^+$ progenitor cells, transit amplifying cells, immature enterocytes,

258 mature enterocytes, BEST4^{+} ionocytes, goblet cells, and enteroendocrine cells, which expressed
259 canonical markers associated with these cell types (**Figure 6A-6C**). As expected, we found that
260 Exp enteroids were enriched in CD24^{+} cells, transit amplifying cells, and immature enterocytes
261 and Dif enteroids were enriched in mature enterocytes, and BEST4^{+} ionocytes and exhibited
262 differences in cell type-specific expression (**Figure 6B, Supplemental Figure 5A, 5B**). We found
263 that *IFNε* was enriched in both mature enterocyte populations, as well as in a population of
264 immature enterocytes (**Figure 6D, Supplemental Figure 6C**). The only other IFN detectable in
265 the dataset was *IFNκ*, which was expressed at very low levels in CD24^{+} cells (**Figure 6D**). IFNε-
266 expressing mature enterocyte populations expressed higher levels of basal ISGs than other cell
267 types (**Figure 6E**). Consistent with the FRT epithelium, IFNε was undetectable in the
268 supernatants of both Exp and Dif enteroids and was only detected by ELISA in the cell lysates of
269 both culture conditions (**Figure 6F**). Next, we analyzed publicly available scRNASeq datasets
270 from human intestine tissue (Burclaff et al., 2022; Triana et al., 2021; Wang et al., 2020), which
271 included diverse cell types including stem cells and transit amplifying cells, enterocytes, BEST4^{+}
272 ionocytes, Tuft cells, enteroendocrine and goblet cells, and immune cells (**Figure 6G, 6H,**
273 **Supplemental Figure 5D**). Consistent with our findings in human enteroids, we found that
274 *IFNε* was expressed in enterocytes (**Figure 6I**). However, these data also suggested that *IFNε* is
275 expressed in transit amplifying cells and Tuft cells (**Figure 6I**). These populations also highly
276 expressed ISGs (**Figure 6J**). Together, these findings indicate that *IFNε* is selectively expressed
277 in specific epithelial cell types within the GI tract and is retained intracellularly, suggesting a
278 potential autocrine role in GI mucosal immunity similar to that observed in the FRT.

279 The basal expression of *IFNε* in the intestinal epithelium suggested that it may contribute
280 to antiviral defenses in the GI tract. To test this, we infected WT and *Ifnε*$^{-/-}$ mice with coxsackievirus
281 B (CVB), an enterovirus that infects via the enteral route. Mice were infected with CVB3 (H3) by
282 oral gavage. We found that *Ifnε*$^{-/-}$ mice lost significantly more weight than WT controls (**Figure 6K**)

283 and had higher rates of death following infection (**Figure 6L**). Notably, viral burdens in secondary
284 organs, including the heart, liver, pancreas, and brain, sites commonly affected by CVB, were
285 markedly elevated in *Ifnε*$^{-/-}$ mice relative to WT controls, indicating enhanced viral dissemination
286 from the intestines to distant tissues (**Figure 6M**). To confirm that these differences were not due
287 to microbiome alterations in WT or *Ifnε*$^{-/-}$ mice, which have been shown to impact CVB infection
288 (Robinson et al., 2019), we conducted 16S rRNA sequencing of the small ribosomal subunit from
289 fecal samples of *Ifnε*$^{+/-}$ and *Ifnε*$^{-/-}$ littermates, thereby controlling for potential cage effects. The
290 resulting dataset contained 2,695 OTUs, excluding those with a total count below three. On
291 average, 76,503 quality-filtered reads were generated per sample, ensuring a robust analysis of
292 microbiome composition (**Supplemental Figure 6A)**. High-quality reads were classified using the
293 Silva v. 138 reference database, and OTUs were aggregated at each taxonomic rank
294 (**Supplemental Figure 6B**). Alpha diversity, measured by the Shannon index, was comparable
295 between *Ifnε*$^{-/-}$ (mean = 4.004, SD = 0.015) and WT (mean = 3.865, SD = 0.262) mice
296 (**Supplemental Figure 6C)**. Differential abundance testing using DESeq2 revealed no OTUs with
297 statistically significant differential abundance between WT and *Ifnε*$^{-/-}$ mice, indicating that
298 microbiome composition was similar across genotypes. Together, these data indicate that IFNε
299 controls enteral viral infections and thus serves as a barrier against systemic viral spread from
300 the GI tract to secondary organs.
301

302 **Discussion**

303 Antiviral defenses at mucosal surfaces are a crucial first-line defense against systemic
304 infection. Type I IFNs play well-established roles in mucosal immunity and are induced by infection
305 to elicit antiviral programs in target cells by signaling through the type I IFN receptor. Although
306 IFNε is a type I IFN that also signals through the type I IFN receptor, it is not induced by infection
307 or PAMPs. IFNε was initially characterized in the epithelium of the FRT where it was proposed to
308 be hormonally regulated, and more recently in the epithelium of the colon, indicating that IFNε

309 has a role in immunity across many epithelial barriers. Here, we showed that IFNε plays a
310 constitutive, essential role in antiviral defenses across multiple mucosal sites. Using an *Ifnε*$^{-/-}$
311 mouse model, we confirmed that IFNε provides innate antiviral protection within the FRT, where
312 it is expressed in specific epithelial cell clusters in a location-dependent manner and is associated
313 with basal expression of ISGs. scRNASeq across the estrous cycle demonstrated that *Ifn*ε
314 expression is not directly regulated by the cycle but instead reflects the distribution of IFNε-
315 expressing epithelial cells. Moreover, we observed that IFNε is retained intracellularly in FRT-
316 derived primary human cells. Extending these findings to the GI tract, we found that IFNε is
317 expressed at high levels in enterocytes of human enteroids and tissue and provides antiviral
318 protection, as *Ifnε-/-* mice showed increased susceptibility to enteric viral infection. Together, these
319 results highlight IFNε as a critical component of mucosal immunity, offering sustained antiviral
320 defense across both reproductive and GI epithelial tissues.

321 IFNε has been primarily studied in the context of the FRT, where it is expressed in the
322 epithelium and has direct antimicrobial and antitumor activity. Using scRNAseq, we further defined
323 the epithelial populations that express *Ifnε* throughout the mouse FRT using an existing single cell
324 atlas of normally cycling mice (Winkler et al., 2024). We found that *Ifnε* is expressed in distinct
325 epithelial cell types in each tissue: luminal and secretory cells in the uterus; columnar cells in the
326 vagina; ciliated cells in the oviducts; and superficial cells in the cervix. In each epithelial population
327 that expressed *Ifnε* we examined its expression levels at each estrous cycle stage. While *Ifnε*
328 expression showed some fluctuations with estrous stage within individual tissues, it was
329 consistently observed at all stages, with no patterns of fluctuation that were consistent across all
330 tissues. The cell types that express *Ifnε* in the uterus; secretory and luminal epithelial cells, make
331 up the layers of the endometrium that expand in preparation for embryo implantation during
332 estrous (Jin, 2019) which could result in the higher gross *Ifnε* transcripts at a tissue level that
333 others have observed in the uterus. These findings refine our understanding of *Ifnε* expression in
334 the FRT, revealing its presence in distinct epithelial populations across tissues and estrous

335 stages, suggesting a stable role in mucosal immunity that adapts to tissue-specific epithelial
336 dynamics, especially in the endometrial layers preparing for implantation.

337 In *Ifnε*$^{-/-}$ mice we observed that IFNε exhibits antiviral activity against the enteric virus
338 coxsackievirus B (CVB) following oral infection. *Ifnε*$^{-/-}$ mice exhibited increased weight loss and
339 mortality following infection which corresponded with higher viral titers in the intestines, heart and
340 liver at 4dpi. Previous studies have identified a role for IFNε in modulating inflammation in colitis
341 models and shown Ifnε expression by IHC in the colon (de Geus et al., 2024). To further define
342 the cell types that express IFNε in the intestine, we analyzed *IFNε* expression in human enteroids
343 and in human intestinal scRNAseq data sets. We used enteroid models cultured under two
344 separate conditions to capture the spread of intestinal cell types in the intestine and found that
345 *IFNε* both in mature and immature enterocytes in both our enteroid and human intestine single
346 cell datasets, as well as in tuft cells in human intestine. Taken together, these data define a role
347 for IFNε throughout the intestines, where it is expressed in enterocytes and controls viral infection.
348 Although IFNε has been observed previously outside of the FRT, our findings reveal its antiviral
349 function in an additional mucosal environment.

350 It is possible that IFNε is expressed at other cellular barriers including the upper and lower
351 airway, blood brain barrier, urinary tract, testes and/or eyes. We initially expected that IFNε-
352 expressing cell types would share common features; however, we observed distinct anatomical
353 differences among the epithelial populations expressing *IFNε*. IFNε has been identified in tissues
354 by IHC and is often found in the epithelial cells lining the lumen of tissues (de Geus et al., 2024;
355 Demers et al., 2014; Fung et al., 2013; Marks et al., 2023). This pattern suggests that IFNε
356 expression may be influenced by specific environmental or spatial triggers within these barriers.
357 Recently, the transcription factor ELF3 was identified as driver of *Ifnε* expression in the mouse
358 uterus (Fung et al., 2024), where it appears to support tissue-specific immune readiness. ELF3 is
359 an epithelium-specific transcription factor involved in regulating the expression of genes essential
360 for barrier function and epithelial integrity. While we consistently observed *Elf3* expression almost

361 exclusively in *Ifnε*-expressing clusters throughout the FRT, in the intestine *ELF3* was detectable
362 in all cell types, indicating that there are other factors that control *IFNε* expression. This finding
363 indicates that distinct transcriptional programs may regulate IFNε expression across different
364 tissues, potentially adapting its expression to localized immune needs and environmental cues.
365 Together, these observations suggest that IFNε expression is not only anatomically specialized
366 but may also be regulated by diverse transcriptional drivers in response to the unique
367 environmental contexts of each barrier tissue.

368 We focused on the direct antiviral effects of IFNε signaling in epithelial cells, but it is likely
369 that IFNε also plays a nuanced role in immune cell signaling. Many groups have reported that
370 immune cells respond to recombinant IFNε treatment by becoming activated, expanding, or
371 upregulating ISGs (de Geus et al., 2024; Garcia-Minambres et al., 2017; Marks et al., 2019). This
372 is not surprising, as type I IFNS can activate or influence virtually all immune cell types. However,
373 it remains to be determined whether IFNε is also retained intracellularly in immune cells, and if
374 basal, intracellular IFNε signaling has distinct effects than exogenous treatment. It has been
375 observed that IFNε knockout mice have reduced NK cells numbers in the uterus, a phenotype
376 that results in part from decreases in IL-15 signaling in *Ifnε*$^{-/-}$ macrophages/monocytes (Mayall et
377 al., 2024). In mouse models of colitis, *Ifnε*$^{-/-}$ mice exhibit decreased levels of T_{regs} in the intestines
378 which exacerbates intestinal pathology (de Geus et al., 2024; Fung et al., 2013). These findings
379 indicate that IFNε likely has a role in regulating resident tissue immune cells as well as those that
380 respond during infection.

381 Although many cell types respond to IFNε after exogenous treatment with recombinant
382 protein, the cellular targets of IFNε signaling have not been well-defined in models where it is
383 basally expressed. In our scRNAseq analyses, we observed ISG expression restricted to cells
384 that also basally expressed IFNε. This ISG expression is dependent on IFNε, as *Ifnε*$^{-/-}$ mice lack
385 ISG expression in the absence of IFNε signaling, suggesting an autocrine role for IFNε. Moreover,
386 in primary human vaginal and uterine epithelial cell lines, we found that IFNε was detectable by

387 ELISA in cell lysates but was undetectable in cell supernatants regardless of viral infection or
388 stimulation. We observed similar results in human enteroids, where IFNε expression could be
389 readily detected by scRNAseq and ELISAs of cellular lysates, but not in supernatants. Taken
390 together, these results indicate that while IFNε is basally expressed, it is retained intracellularly
391 and exerts an antiviral effect in epithelial cells through autocrine signaling. The exact mechanism
392 by which IFNε signals to cells without being secreted remains unclear, but several possible
393 explanations can be considered. For example, the type I IFN receptor is endocytosed immediately
394 after binding IFNs, allowing JAK/STAT signaling to continue within the endosome (Zanin et al.,
395 2020). This suggests that IFNε may activate the type I IFN receptor intracellularly, possibly within
396 endosomal compartments. Future studies will be crucial in elucidating the precise intracellular
397 mechanisms by which IFNε initiates signaling and identifying the specific cellular contexts where
398 its autocrine activity plays a protective role, which may provide new insights into its unique function
399 at mucosal barriers.

400 Unchecked interferon responses can lead to debilitating autoimmune diseases and post
401 infection pathology, highlighting the need for regulation of a constitutively expressed interferon.
402 Retaining IFNε intracellularly within specific epithelial layers vulnerable to infection may prevent
403 aberrant immune activation while still providing basal antiviral protection. However, in cases of
404 cellular damage or viral infection, IFNε could also function as a damage-associated molecular
405 pattern (DAMP). Upon epithelial cell damage or lysis, IFNε may be released into the extracellular
406 space, where it could act in a paracrine manner to signal neighboring mucosal cells or immune
407 cells. This release could enhance local immune responses and alert surrounding tissues to
408 infection or injury, promoting a targeted antiviral response while still limiting widespread immune
409 activation.

410 Together, our findings underscore the unique role of IFNε in maintaining mucosal immunity
411 as a constitutively expressed, intracellularly-retained IFN within epithelial barriers. By providing
412 baseline antiviral protection while remaining poised for activation upon cellular damage or

413 infection, IFNε serves as both a steady immune defender and a potential DAMP, capable of
414 alerting neighboring cells to pathogenic threats. This dual functionality helps prevent unwanted
415 immune activation that could lead to autoimmune pathology, while ensuring rapid and localized
416 antiviral responses when needed. Future studies aimed at clarifying the intracellular signaling
417 mechanisms of IFNε and its DAMP-like functions may reveal new therapeutic approaches for
418 enhancing mucosal immunity without triggering systemic inflammation.
419

420 **Acknowledgments**
421 This work was supported by R01AI081759 (C.B.C). N.S.H is funded in part by R01AI168107. We
422 thank the Duke University School of Medicine for the use of the Sequencing and Genomic
423 Technologies Shared Resource, which provided RNA-seq services.
424

425 **Methods**

426 **Generation of IFNε Knockout Mice Using iGONAD**

427 IFNε knockout (*Ifnε*$^{-/-}$) mice were generated using the Genome Editing via Oviductal Nucleic Acid
428 Delivery (iGONAD) technique, as previously described (Ohtsuka et al., 2018; Skavicus and
429 Heaton, 2023). Briefly, female C57BL/6J mice were mated with C57BL/6J males. On the morning
430 of day E0.7, CRISPR/Cas9-mediated gene editing was performed on pregnant mice by injecting
431 a ribonucleoprotein (RNP) complex consisting of Cas9 protein and two guide RNA (gRNAs)
432 targeting exon 1 (AACGGATTCCCTTCCAATTG[TGG] and
433 AAGTCTTAGCTGCGCTTCAC[CGG], where the PAM sites are indicated with [PAM]) of the *Ifnε*
434 gene into the oviducts. The two gRNAs were designed to flank and induce double-strand breaks,
435 leading to the deletion of a 263 basepair fragment within exon 1, which resulted in a frameshift
436 mutation and knockout of IFNε expression. After injection, the oviducts were electroporated to
437 facilate the delivery of the ribonucleoprotein (RNP) complex into presumed one-cell stage
438 zygoyes. After gene editing surgery, embryos continued to develop, and pregnant females were

439 allowed to deliver naturally. Genotyping of the resulting pups was carried out by extracting
440 genomic DNA from toe biopsies using a lysis buffer containing 50 mM Tris-base (pH 8.0), 50 mM
441 KCl, 2.5 mM EDTA, 0.45% IGEPAL CA-630 (NP40), 0.45% Tween-20, and 20 mg/mL proteinase
442 K, followed by incubation at 94°C for 10 minutes. PCR amplification was performed with primers
443 flanking the gRNA target sites (forward: AGACAAGTGCACAGTGAAGCCA; reverse:
444 TCCGCCACCAACCTATGTCTTTC) using TITANIUM Taq DNA Polymerase (Takara). The
445 knockout was further confirmed by Sanger sequencing using a primer upstream of the gRNA sites
446 (TCCCAGAACTGGAGTGGT) to verify successful deletion of the *Ifnε* gene. Ifnε$^{-/-}$ mice were
447 backcrossed to C57BL/6J for at least six generations before use in experiments to establish a
448 stable knockout line. Once established, Transnetyx developed a custom qPCR-based genotyping
449 assay to streamline the identification of *Ifnε* knockout alleles in subsequent generations.
450

451 **Viruses**

452 HSV-2 (strain 333) was provided by Helen Lazear (University of North Carolina at Chapel Hill)
453 and propagated and titrated using a plaque assay in Vero cells, which were cultured in Dulbecco's
454 Modified Eagle Medium (DMEM) supplemented with 5% fetal bovine serum (FBS). CVB3 (H3
455 strain) (Hardy et al., 2004) were propagated and titrated in HeLa cells cultured in Modified Eagle'
456 s Medium (MEM) supplemented with 5% FBS. For titration, serial dilutions of virus were added to
457 Vero (HSV-2) or CVB3 (HeLa) cell monolayers and incubated for 1 day at room temperature.
458 Following binding, cells were overlaid with a mixture of phenol red-free MEM and 0.5% agarose
459 and incubated for 48-72hrs at 37°C and 5% CO_2. The overlay was removed after incubation and
460 plaques were subsequently visualized by staining with crystal violet. Sendai virus (Cantell Strain)
461 was purchased from Charles River (PI-1, SV).
462

463 **HSV-2 infections**

464 8–10-week-old virgin female mice were used for all experiments. For HSV-2 infections females
465 were treated with 2mg of MPA (MedroxyProgesterone Acetate, NDC 66993-270-83) by
466 subcutaneous injection 5 days prior to infection to synchronize females in diestrus. Diestrus was
467 confirmed by vaginal cytology as previously described(Byers et al., 2012) 100 or 10,000 PFU of
468 HSV-2 was given by vaginal inoculation in a 10uL volume. HSV-2 was diluted in sterile PBS. Mice
469 were weighed and scored for pathology daily according to the following criteria: 0 no inflammation;
470 1 vaginal edema and redness; 2 hair loss or ulceration localized to the vaginal-anal area; 3 severe
471 ulceration, extensive hair loss extending beyond the vaginal-anal area; 4 overt disease signs; 5
472 paralysis; 6 death. Vaginal washes were taken by pipetting 110uL of PBS in and out of the vagina
473 5 times. Vaginal lavages were titrated by plaque assay on Vero cells as described above.
474

475 **CVB-H3 infections**

476 All CVB-H3 infections were performed in 8–10-week-old male mice. Mice were infected by oral
477 gavage with 1x10^8 pfu in 100uL of PBS. For viral burden experiments mice were sacrificed after
478 4 days, tissues were harvested and homogenized in DMEM using an Omni International Bead
479 Ruptor Elite (19-042E) at 4m/s for 1 minute using 2.8mm ceramic beads in 2 ml tubes (Omni
480 International 19-628). Viral burdens were quantified using a $TCID_{50}$ assay on HeLa cells. Serial
481 ten-fold dilutions of virus samples were prepared in complete medium and added to confluent
482 monolayers of HeLa 7B cells in 96-well plates. Cells were incubated for 3 days (37°C, 5% CO_2).
483 Cells were fixed and stained with crystal violet to visualize cytopathic effect (CPE). The dilution at
484 which 50% of wells showed CPE was recorded as the $TCID_{50}$ endpoint, using the Reed-Muench
485 method to calculate the viral titer.
486

487 **Generation of uterine single-cell suspension for scRNASeq**

488 Naturally cycling WT and IFNE mice in estrus were confirmed by vaginal cytology (Byers et al.,
489 2012). The whole uterus was dissected and placed in 1x DPBS on ice until all tissues were

490 harvested. Uteruses were minced into 1-2mm pieces with dissecting scissors and placed into
491 2.5mL of D-PBS supplemented with Ca and Mg (Gibco, 14040117). Once all tissues were minced,
492 2.5 mLs of pre-warmed 2x disassociation media was added. 2x disassociation media was made
493 by dissolving 4mg/mL of Collegnase A (Roche, 10103578001) and 2U/mL of DNAase I (Roche
494 04536282001) in dispase (Corning 354235). Samples were incubated for 30 minutes at 37
495 degrees and were shaken vigorously for 30 seconds every 5 minutes. After incubation, enzymes
496 were inactivated by adding 0.5mL of FBS and samples placed on ice. Samples were pushed
497 through 100um filter (VWR 732-2759) using a plunger of a 1mL syringe. Cells were pelleted at
498 400g for 3 minutes at 4C and resuspended in 1mL of ice-cold PBS. 2ml of RBC lysis buffer
499 (Invitrogen, 00-4333-57) was added for 1 minute with a single inversion to mix, and then 10mLs
500 of 1% FBS-DPBS was added to each sample. Cells were pelleted at 400g for 3 minutes at 4C
501 and resuspended in 500uL of ice cold 1% FBS-PBS. Cells were counted and resuspended at a
502 final volume of $1.5x10^6$ cells/mL in 1% FBS-DPBS. Cells were kept on ice immediately dropped
503 off for scRNAseq processing.
504

505 **Enteroid Growth and Single Cell Preparation**

506 Human fetal enteroid culture and differentiation were based on published protocols for adult stem
507 cells (Beumer et al., 2022; He et al., 2022; Pleguezuelos-Manzano et al., 2020). For expansion,
508 enteroids were passaged by single-cell dissociation in TrypLE (Gibco) at 37°C for 5 min,
509 resuspended in 40 µl Matrigel (Corning) domes, and overlayed with expansion medium (ExM) for
510 7 days. For differentiation, enteroids were mechanically disrupted in DPBS, resuspended in 40 µl
511 Matrigel domes, grown in patterning medium (PaM) for 16 days and in differentiation medium
512 (DiM) for 3 days. For single-cell analysis, enteroids were expanded (Exp) or differentiated (Dif),
513 scraped into cold DPBS, pelleted 5 min at 400 xg, resuspended in TrypLE, and incubated at 37°C
514 for 15 min. Enteroids were mechanically dissociated by pipetting up and down 30 times, diluted
515 in basal media, pelleted 5 min at 400 xg, resuspended in DPBS with 1% BSA, and filtered through

516 a 30 µm strainer. Basal media contained: 10 mM HEPES, 2 mM L-glutamine, and 100 U/ml
517 penicillin-streptomycin in Advanced DMEM/F12 (Gibco). Expansion media (ExM) additionally
518 contained: 1X B27 (Invitrogen), 1 mM N-acetylcysteine (Sigma), 50 ng/ml mouse EGF
519 (Peprotech), 100 ng/ml mouse Wnt3a, 500 ng/ml mouse R-Spondin, 100 ng/ml human noggin
520 (R&D Systems), 1x N2 (Invitrogen), 10 mM Nicotinamide (Sigma), 100 ng/ml human IGF-1, 50
521 ng/ml human FGF-2 (Peprotech), 500 nM A83-01 (Tocris), 10 nM PGE2 (R&D Systems), and 10
522 nM [leu15]-Gastrin I (Millipore). Patterning media (PaM) additionally contained: 1X B27, 1 mM N-
523 acetylcysteine (NAC), 50 ng/ml mouse EGF, 100 ng/ml mouse Wnt3a, 500 ng/ml mouse R-
524 Spondin, 100 ng/ml human noggin, 500 nM A83-01, and 2 ng/ml IL-22 (Peprotech). Differentiation
525 media (DiM) additionally contained 1X B27, 1 mM N-acetylcysteine (NAC), 50 ng/ml mouse EGF,
526 50 ng/ml BMP-2 and 50 ng/ml BMP-4 (Peprotech).
527

528 **Single-Cell RNA-seq Library Preparation and Data Analysis**

529 Publicly available datasets from cycling mouse tissue (Winkler et al., 2024) were downloaded
530 from ArrayExpress (E-MTAB-11491 and from human intestine were downloaded from GEO
531 (accession numbers: GSE185224, GSE171620, GSE125970) (Burclaff et al., 2022; Triana et al.,
532 2021; Wang et al., 2020). For uterus tissue from WT and *Ifnε*$^{-/-}$ mice, single-cell RNA-seq libraries
533 were prepared from ~10,000 cells/mouse using the 10x Genomics Chromium Single Cell 3'
534 Reagent Kit (v2 chemistry, Manual Part #CG00052) following the manufacturer's protocol. Briefly,
535 single-cell suspensions were loaded into the 10x Chromium Controller to capture and barcode
536 individual cells. Libraries were constructed, and sequencing was performed on an Illumina
537 NovaSeq 6000 system (Illumina, San Diego) using an S2 flow cell, providing an average
538 sequencing depth of ~61,000 reads per cell. After sequencing, raw base call (BCL) files were
539 processed with the 10x CellRanger pipeline (v6.1.2, 10x Genomics) for demultiplexing, alignment
540 to the mouse reference genome (GRCm38), and quantification of gene expression. Quality control
541 and post-processing were carried out using the CellRanger count and aggregate functions to

542 generate gene expression matrices. Data analysis was performed using the Seurat package
543 (Hafemeister and Satija, 2019; Satija et al., 2015) (v4.0) in R. Cells were filtered to include those
544 with at least 700 but no more than 12,000 unique expressed genes. Additionally, cells with over
545 10% mitochondrial gene content were excluded from further analysis. To correct for batch effects,
546 datasets from individual animals were normalized using the SCTransform() function (v2) in Seurat,
547 and integration was performed using the FindIntegrationAnchors() and IntegrateData() functions.
548 Dimensionality reduction was conducted via principal component analysis (PCA) using the
549 RunPCA() function.Cell clusters were identified using Louvain clustering with the FindClusters()
550 function in Seurat. The optimal clustering resolution was determined by evaluating clustering
551 stability across a range of resolutions (0.2 to 1.0) using the clustree() package, with a resolution
552 of 0.3 selected for downstream analysis. For combined analyses of wild-type (WT) and *Ifnε*$^{-/-}$
553 datasets, previously integrated datasets were merged and further integrated using the Harmony
554 algorithm (Korsunsky et al., 2019) (v1.0) for batch correction and alignment. Differential
555 expression analysis between clusters was performed using the Wilcoxon rank sum test
556 implemented in Seurat's FindAllMarkers() function. Genes with a log2 fold change > 0.25 and an
557 FDR-adjusted p-value < 0.05 were considered significantly differentially expressed. Marker genes
558 for each cluster were identified by searching for positively enriched genes using the
559 aforementioned criteria.

560 Human fetal enteroid single-cell RNA-seq libraries were similarly prepared, sequenced
561 and analyzed with minor differences. ~10,000 cells/sample were targeted, providing an average
562 sequencing depth of ~61,000 reads per cell. After sequencing, BCL files were processed with the
563 10x CellRanger pipeline (v7.0.1, 10x Genomics) for demultiplexing, alignment to the human
564 reference genome (GRCh38), and quantification of gene expression. Cells were filtered to include
565 those with at least 3,000 but no more than 10,000 unique expressed genes. Cells with less than
566 2% or more than 20% mitochondrial gene content were excluded from further analysis. Individual
567 samples were merged and integrated using the FindIntegrationAnchors() and IntegrateData()

568 function into Exp and Dif. Percent mitochondrial genes, feature count, read count, and the
569 difference of G2M and S phase scores were regressed. For combined analysis, Exp and Dif were
570 merged and further integrated using the Harmony algorithm (Korsunsky et al., 2019) (v1.0) for
571 batch correction and alignment.

572 Human intestinal tissue datasets were downloaded and cells filtered to include those with
573 at least 1,000 but no more than 10,000 unique expressed genes. Cells with less than 2% or more
574 than 25% mitochondrial gene content were excluded from further analysis. Cells from regions
575 outside the small intestine were excluded. Individual samples were merged using the
576 FindIntegrationAnchors() and IntegrateData() function. Percent mitochondrial genes, feature
577 count, read count, and the difference of G2M and S phase scores were regressed. All files
578 associated with this single-cell RNA-seq study have been deposited in the Gene Expression
579 Omnibus (GEO).

580

581 **Primary cells**

582 Primary human cells were purchased from Lifeline Cell Technologies (FC-0078, FC-0083) and
583 thawed into 24-well or 6-well plates according to manufacturer instructions. At 90% confluency
584 cells were treated with PAMPS or infected at the following concentrations; polyIC float (Invivogen,
585 tlrl-picw) 10ug/mL; polyIC transfection (Inviogen, tlrl-picw) 1ug/mL (0.5ug/well); cGAMP
586 transfection (Invivogen, tlrl-nacga23-02) 10ug/mL; SeV Cantell 20HAU well; HSV-2 333 MOI of
587 1; LPS float (invivogen, tlrl-eklps) 100ng/mL. cGAMP and polyIC transfected using
588 xTREMEgene9 (Roche, XTG9-RO) according to manufacturer's instructions.

589

590 **qPCR and bulk RNA Sequencing**

591 RNA was extracted from cells using Qiagen Rneasy mini kit (74104) according to
592 manufacter instructions. *IFNε*, *IFNβ*, and *ACTB* RNA levels were detected by qRT-PCR using IDT
593 PrimeTime Std qPCR Assay Primer Probes: *IFNε* Hs.PT.58.4812867; *IFNβ1*

Hs.PT.58.39481063.g, ACTB: Hs.PT.39a.22214847 and Itaq one step kit (BIO-RAD 172-5140). qRT-PCR was run using a Biorad Opus. For bulk RNA sequencing, libraries were prepared by the Duke Center for Computational Biology and Genomics (GCB) using a mRNA standed KAPA hyperprep kit. Sequencing was performed an Illumina Novaseq X Plus using 100bp paired end sequencing and targeting 10 billion reads across all samples Reads were aligned to the human genome using Qiagen CLC Genomics (v20). Differential expression analysis was performed using DESeq2. Briefly, raw count data were imported into R and DESeq2 (Love et al., 2014) was used to normalize counts and identify differentially expressed genes between specified conditions. Genes with an adjusted p-value < 0.05 and log2 $\pm$ 2 fold change were considered significantly differentially expressed.

ELISA

IFNε and IFNβ protein levels were detected by ELISA (R&D Systems, DY9667-05, DY814-05). IFNε and IFNβ levels were normalized to total protein quantified by Pierce BCA Assay (23227). Cellular lysates were generated using M-PER Mammalian Protein extraction reagent (Thermo Scientific 78501).

16S Ribosomal Sequencing

Fecal samples were collected from adult *Ifnε*$^{+/-}$ *and Ifne*$^{-/-}$ littermates and sent to Microbiome Insights for 16S sequencing and analysis. Specimens were placed into a MoBio PowerMag Soil DNA Isolation Bead Plate. DNA was extracted following MoBio's instructions on a KingFisher robot. Bacterial 16S rRNA genes were PCR-amplified with dual-barcoded primers targeting the V4 region (515F 5'-GTGCCAGCMGCCGCGGTAA-3', and 806R 5'-GGACTACHVGGGTWTCTAAT-3'), as previously described (Kozich et al., 2013). Amplicons were sequenced with an Illumina MiSeq using the 300-bp paired-end kit (v.3). Sequences were denoised, taxonomically classified using Silva (v. 138) as the reference database, and clustered

620 into 97%-similarity operational taxonomic units (OTUs) with the mothur software package (v.
621 1.44.1) (Schloss et al., 2009), following the recommended procedure
622 (https://www.mothur.org/wiki/MiSeq_SOP; accessed Nov 2020). Alpha diversity was estimated
623 with the Shannon index on raw OTU abundance tables after filtering out contaminants. The
624 significance of diversity differences was tested with ANOVA or linear mixed model depending on
625 the study design. To estimate beta diversity across samples, we excluded OTUs occurring with a
626 count of less than 3 in at least 5 % of the samples and then computed Bray-Curtis indices. We
627 visualized beta diversity, emphasizing differences across samples, using Principal Coordinate
628 Analysis (PCoA) ordination. Variation in community structure was assessed with permutational
629 multivariate analyses of variance (PERMANOVA) with treatment group as the main fixed factor
630 and using 999 permutations for significance testing.A dot-dash circle in ordination plot represent
631 for the central of each cluster (Nguyen et al., 2020). All analyses were conducted in the R
632 environment.
633

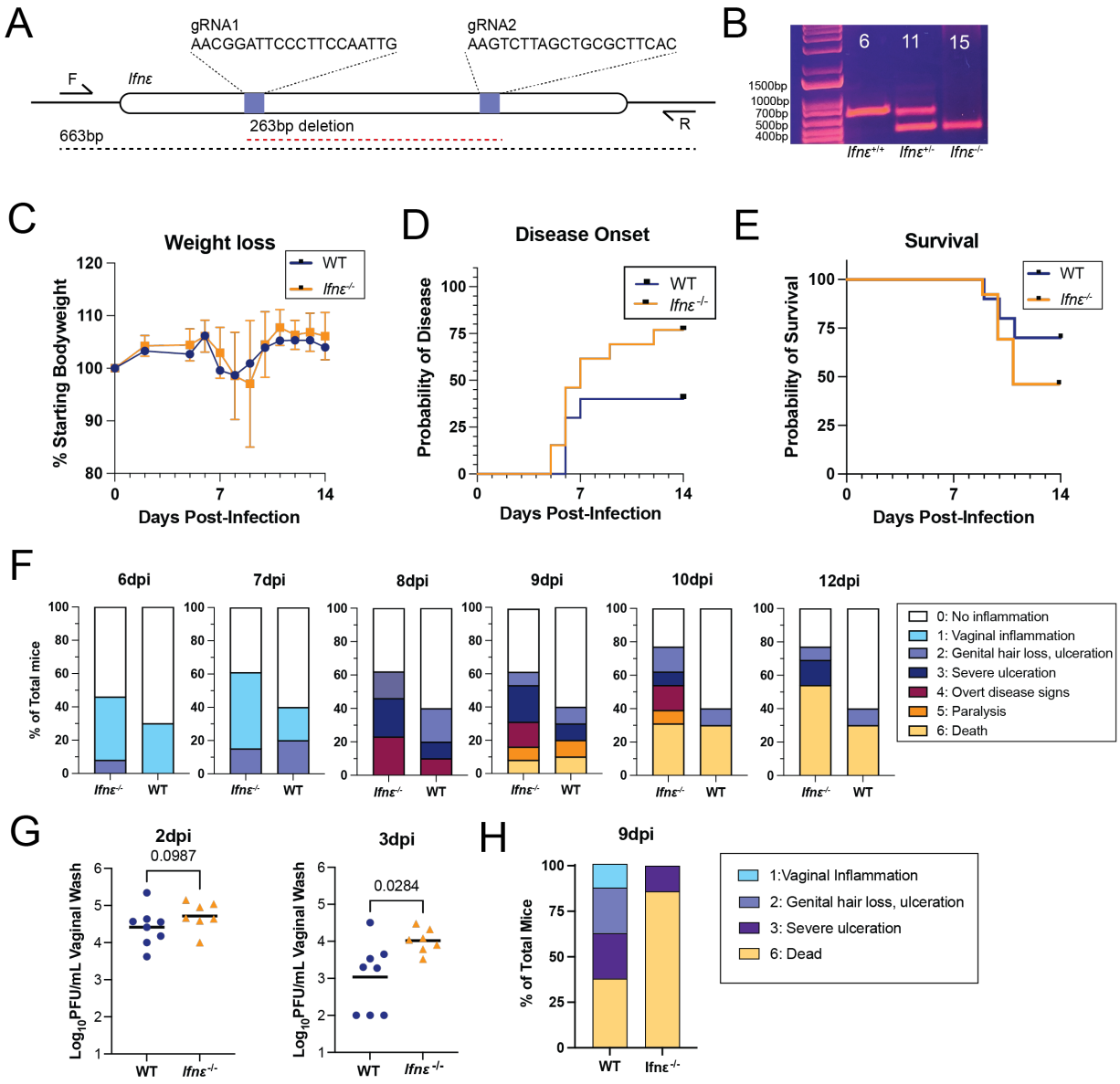

Figure 1: Increased HSV-2 susceptibility in *Ifnε* deficient mice generated via iGONAD CRISPR/Cas9. A) Schematic of CRISPR/Cas9 knockout strategy. **B)** Representative PCR genotyping results from the first generation of pups born to dams that underwent iGONAD gene editing. Mouse 6 (*Ifnε*$^{+/+}$), 11 (*Ifnε*$^{+/-}$) and 15 (*Ifnε*$^{-/-}$) are shown. Mouse 15 was chosen as the founding sire for the line. **C-F)** WT and *Ifnε*$^{-/-}$ females were infected with 100PFU of HSV-2 333 and weighed and monitored for disease signs daily. Weight loss (C), disease onset (D), and survival (E) are shown. Disease onset (D) includes any observable pathology score. In (F), clinical scores are shown at multiple days post-infection (dpi) from 6-12dpi. Key at right. **G-H).**

643 WT and *Ifnε*$^{-/-}$ females were infected with 10,000PFU of HSV-2 333. Vaginal lavages were
644 collected at 2 and 3dpi and titrated by plaque assay. Significant differences were calculated by
645 T-test in Graphpad Prism. Individual animals are depicted by symbols in (G).
646
647
648
649
650
651
652
653
654
655

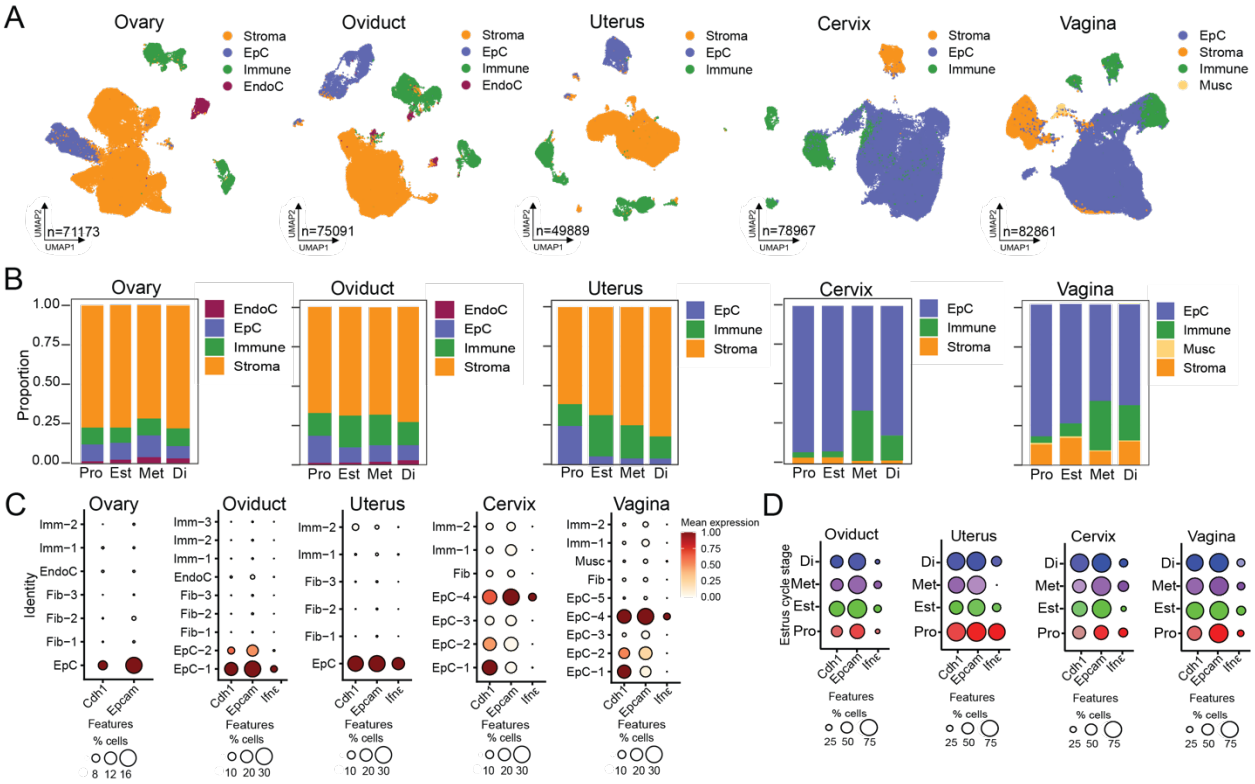

Figure 2: *Ifnε* is expressed in epithelial cells of the female reproductive tract throughout the estrous cycle. A) UMAPS showing clustering of stromal (Stroma, orange), epithelial (EpC, blue), immune (Immune, green), endothelial (EndoC, red), and muscular (Musc, yellow) cells within the different tissues of the female reproductive tract (FRT). **B)** The proportions of each cell type split by estrous stage: Proestrous (Pro); Estrous (Est); Metestrous (Met), and Diestrous (Di). **C-D)** DotPlots showing expression of epithelial cell markers and *Ifnε* in all clusters **(C)** or only in clusters that express *Ifnε* split by estrous stage **(D).**

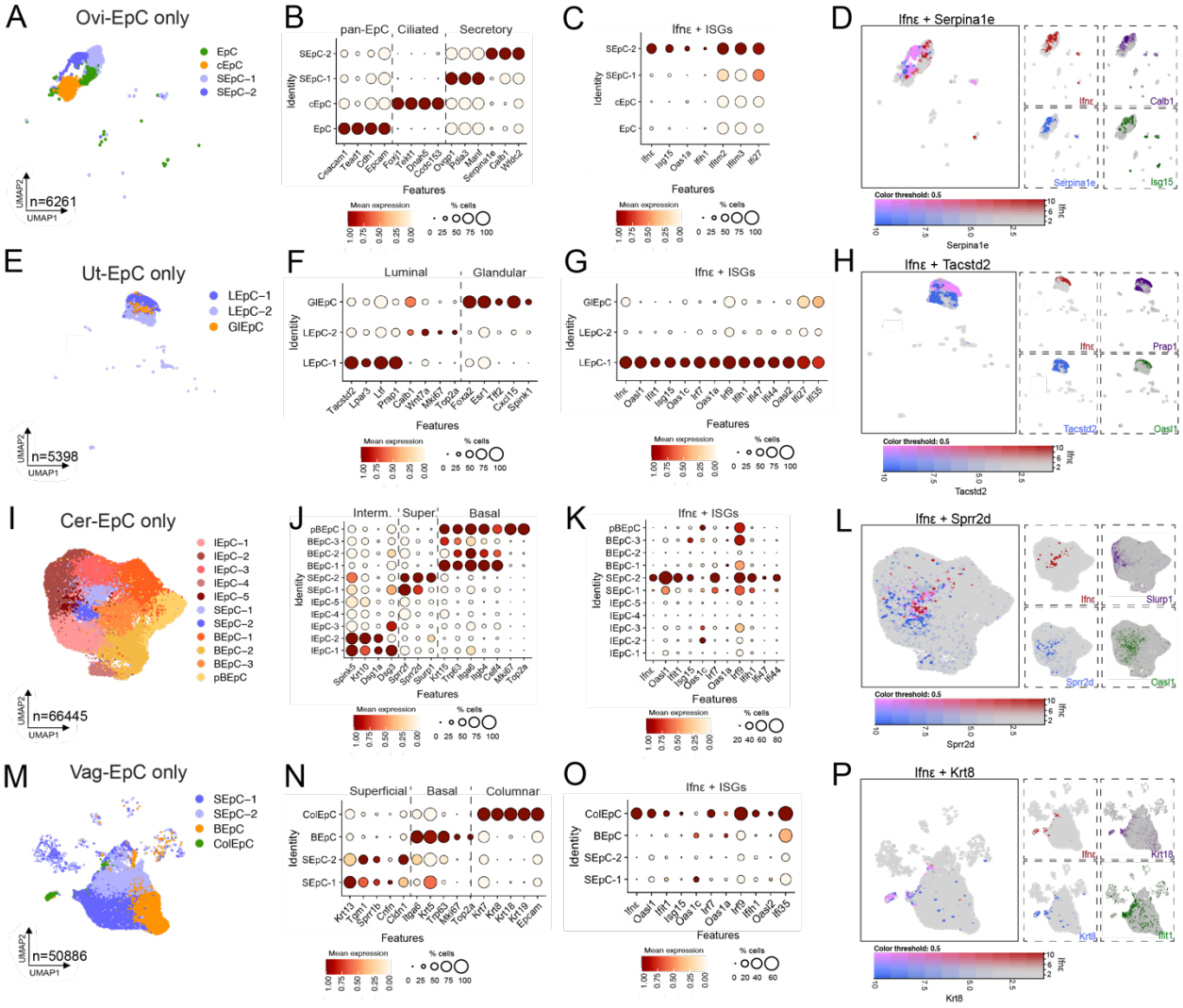

Figure 3*: Ifnε* expression correlates with ISG expression in anatomic site-specific epithelial cells. Epithelial cell clusters from Figure 2 were reclustered. **A,E,I,M)** UMAPS showing clustering of epithelial cell types within each tissue. Oviduct **(A)**: general epithelial cells (Epc), ciliated epithelial cells (cEpC), and secretory epithelial cells (SEpC-2). Uterus **(E)**: luminal epithelial cells (LEpC) and glandular epithelial cells (GlEpC). Cervix **(I)**: intermediate epithelial cells (IEpC), superficial epithelial cells (SEpC), basal epithelial cells (BEpC), and parabasal epithelial cells (pBEpC). Vagina **(M)**: superficial epithelial cells (SEpC), basal epithelial cells (BEpC), and Columnar epithelial cells (ColEpC). **B,F,J,N).** Dot plots showing markers of each epithelial

subpopulation. **C,G,K,O)** Dot plot showing Ifnε and ISG expression within each cluster. **D,H,L,P)** Feature plots showing expression and coexpression of Ifnε and a top marker for the cluster in which it is expressed.

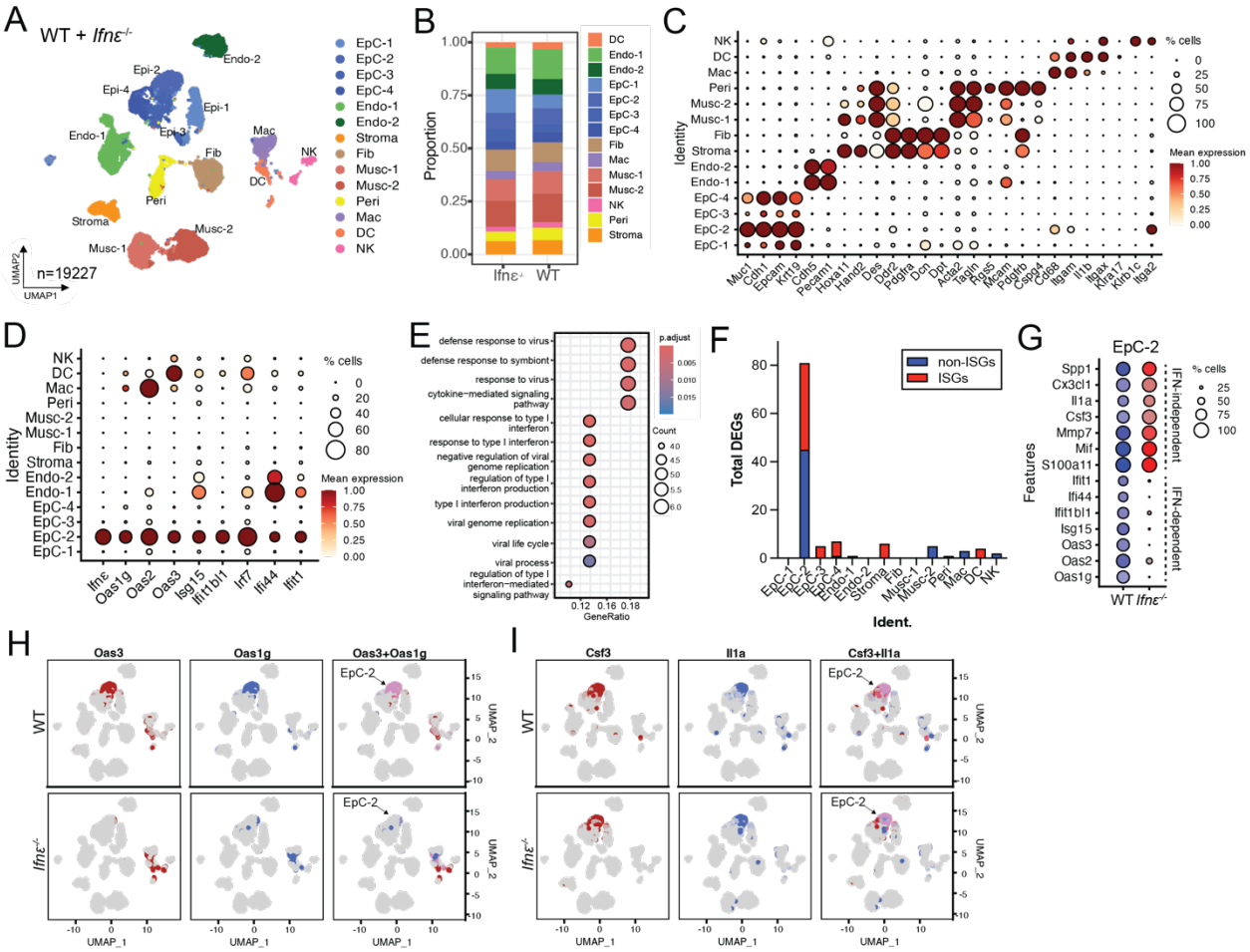

Figure 4. *Ifnε*$^{-/-}$ mice lack basal ISG expression in select uterine epithelial cells. A) UMAPs showing uterine cell clusters from *Ifnε-/-* and WT mice. **B)** Bar plot of the proportions of each cell cluster in *Ifnε-/-* and WT mice. **C)** DotPlot of canonical cell type markers in each cell cluster. Key and scale at right. **D)** DotPlot of *Ifnε* and ISG expression in each cell cluster. Key and scale at right. **E)** Pathway analysis on differentially expressed genes in *Ifnε-/-* and WT uteruses. Shown are the gene counts per pathway and the p-value of each pathway. **F)** The total number of DEGS in each cluster. ISGs are shown in red and non-ISGs are shown in blue. **G)** DotPlot showing ISG and cytokine expression levels split by mouse genotype. Scale at right. **H)** FeaturePlots showing co-expression of *Oas3* and *Oas1g* in either WT (top) or *Ifnε*$^{-/-}$ (bottom) samples. **I)** FeaturePlots showing co-expression of *Csf3* and *Il1a* in either WT or *Ifnε*$^{-/-}$ samples.

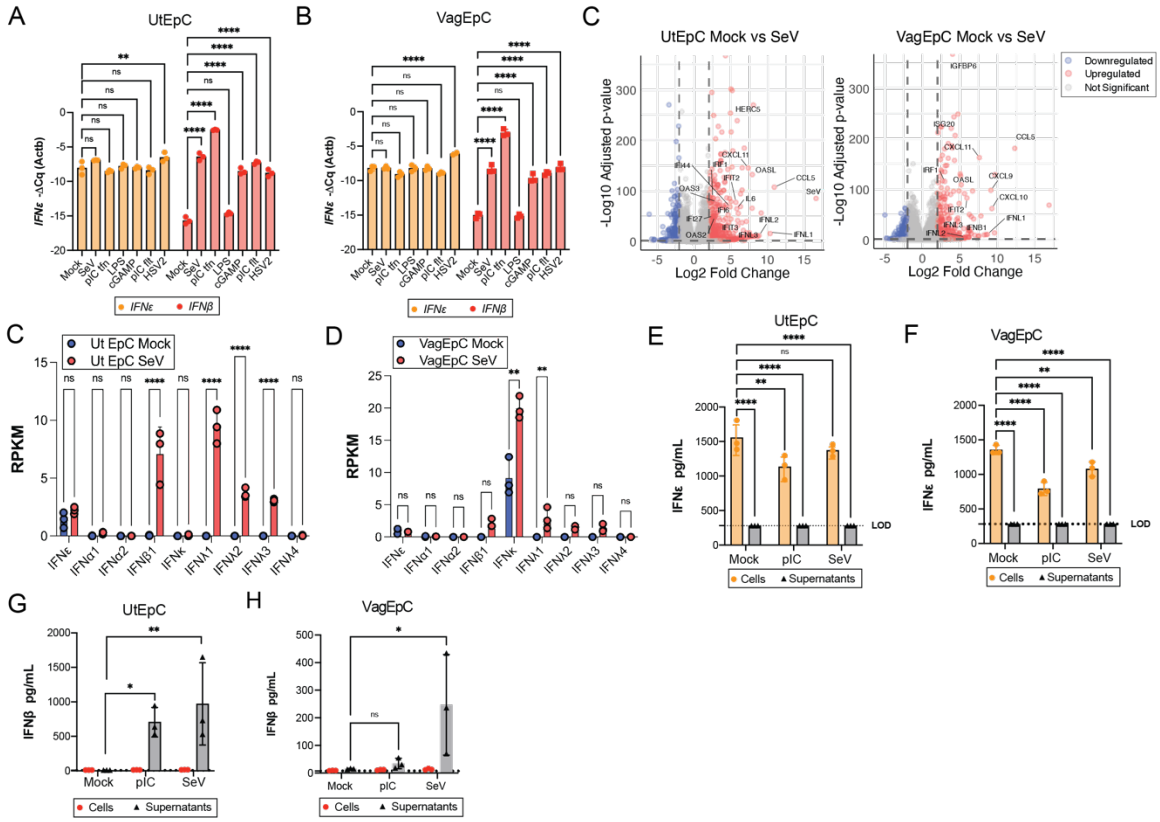

Figure 5: IFNε is retained intracellularly in primary human epithelial cells and is not induced by viral infections. **A, B),** Primary human uterine (UtEpV) (A) or vaginal (VagEpC) (B) epithelial cells were treated infected with Sendai virus cantell (SeV, 200HAU) or HSV2 (MOI of 1), treated with LPS or poly(I:C), or transfected with cGAMP or poly(I:C). Cells were harvested 20hpi and *IFNE* and *IFNB* levels were quantified by qRT-PCR. **C),** Volcano plots of differentially expressed genes ($\log_2 \geq 2$ or ≤ -2, $p_{adj} \leq 0.01$) in UtEpC (left) or VagEpC (right) infected for ~24hrs with 200HAU SeV. Upregulated genes are shown in red and downregulated genes are shown in blue. Select gene names are shown in black. **D, E),** Reads per kilobase of transcript, per million mapped reads (RPKM) of the indicated IFN gene in Mock- (blue) or SeV-infected (red) UtEpC (D) or VagEpC (E). **F-I),** IFNε(F, G) and IFN-β (H, I) protein levels were measured from cell lysates and cell supernatants from uterine (F, H) or vaginal (G, I) epithelial cells by ELISA . Significance was determined by two-way ANOVA using a Tukey's test for multiple comparisons (*, p<0.05, **p<0.01, ***p<0.001, ****p<0.0001, ns ,not significant).

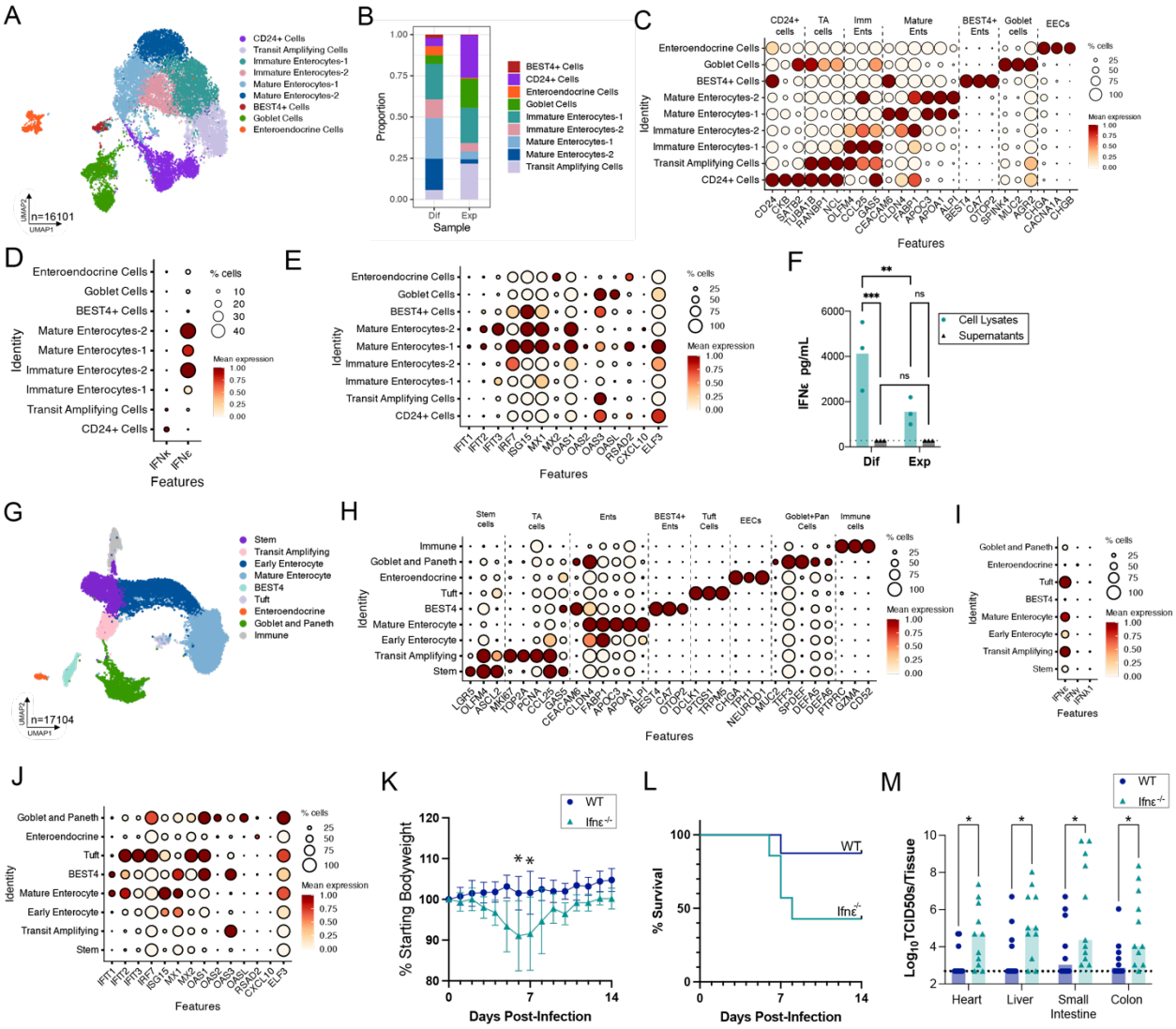

Figure 6: *IFNε* is expressed in the epithelium of the GI tract and protects against enteric viral infections. (A-F), Human enteroids were grown under expansion (Exp) or differentiating conditions (Dif) and then analyzed by scRNAseq. **A)** UMAP plot depicting distinct cell clusters identified in the dataset. Each cluster is represented by a unique color, indicating cellular heterogeneity and grouping based on transcriptomic profiles. **B)** Bar plot depicting cell enrichment under Exp or Dif conditions. **C),** DotPlot of canonical cell makers used to define clusters. Key and scale at right. **D)** *IFNε* and *IFNκ* expression in cell clusters. **E)** DotPlot of ISGs and ELF3 Key and

722 scale at right. **F)** IFNε levels in supernatants and cell lysates from Exp and Dif enteroids,
723 measured by ELISA. Data points represent IFNε concentration across experimental conditions,
724 with significance determined by two-way ANOVA followed by multiple comparisons to assess
725 differences between groups (ns, not signficiant, **p<0.01, ***p<0.001). **G)** UMAP showing cell
726 clusters from human intestinal samples analyzed by scRNAseq. **H)** DotPlot of canonical cell
727 makers used to define clusters. Scale and key at right. **I)** DotPlot of *IFNε, IFNγ*, and *IFNλ1*
728 expression in cell clusters. Scale and key at right. **J)** DotPlot of ISGs and ELF3 Key and scale at
729 right. **K-M)** WT and *Ifnε*$^{-/-}$ mice were orally infected with $1x10^8$ PFU of CVB-H3 and weighed and
730 monitored daily for signs of illness (K,L), or sacrificed at 4 days post infection (dpi). Viral burdens
731 in tissues (M) were determined by TCID50. Significant differences in weight (*p<0.05) were
732 calculated by t-test in Graphpad Prism. Differences in viral burden were calculated by Mann-
733 Whitney test (*p<0.05).

734
735
736
737
738
739
740
741
742
743
744
745
746
747
748
749
750
751
752
753
754
755
756
757
758
759
760

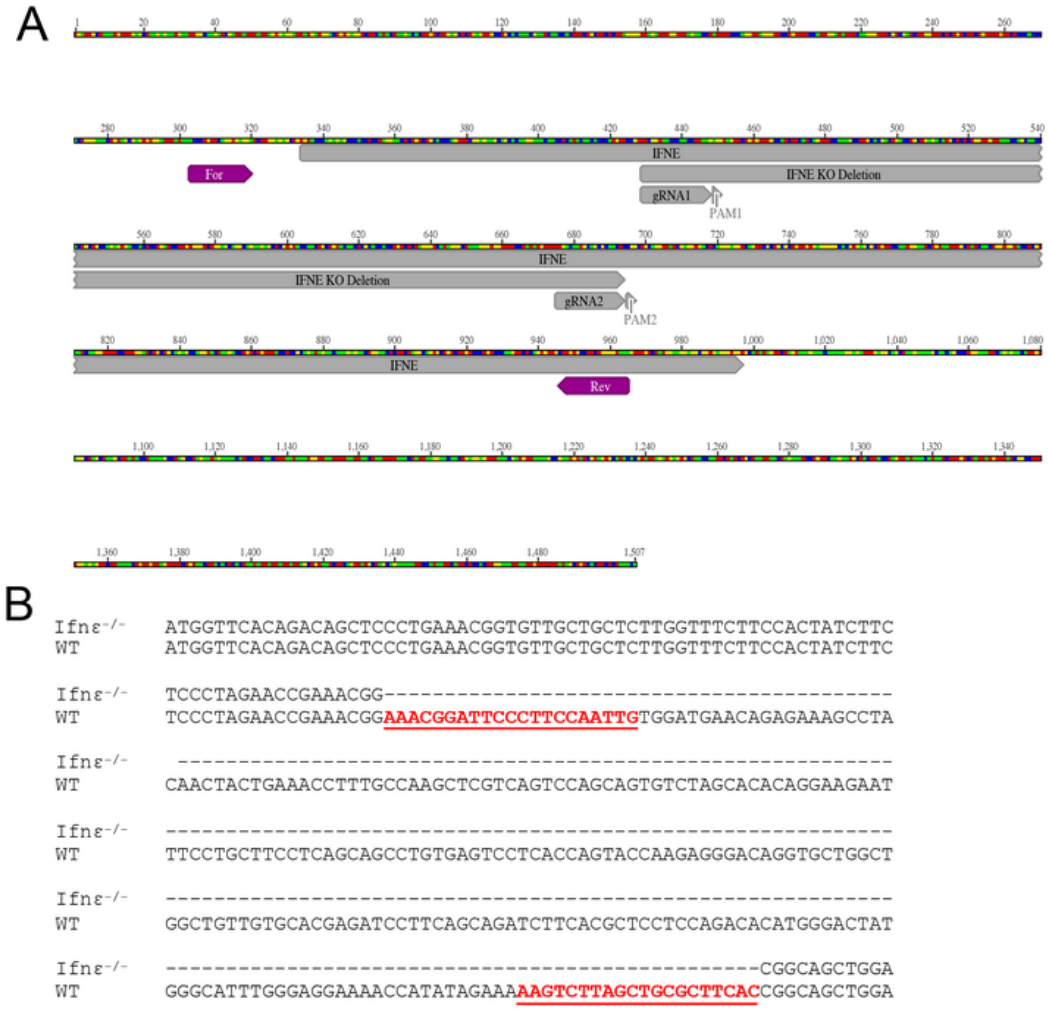

Supplemental Figure 1. (A) Diagram of Ifnε gene, guide RNAs, primers and deleted region. **(B)** Sequence alignment following Sanger sequencing of genomic DNA isolated from an *Ifnε*$^{-/-}$ mouse (top) or wild-type (WT, bottom) mouse. Bold red sequences denote location of gRNAs (gRNA1 and gRNA2). Dashes denote sequence missing in the *Ifnε*$^{-/-}$ mouse.

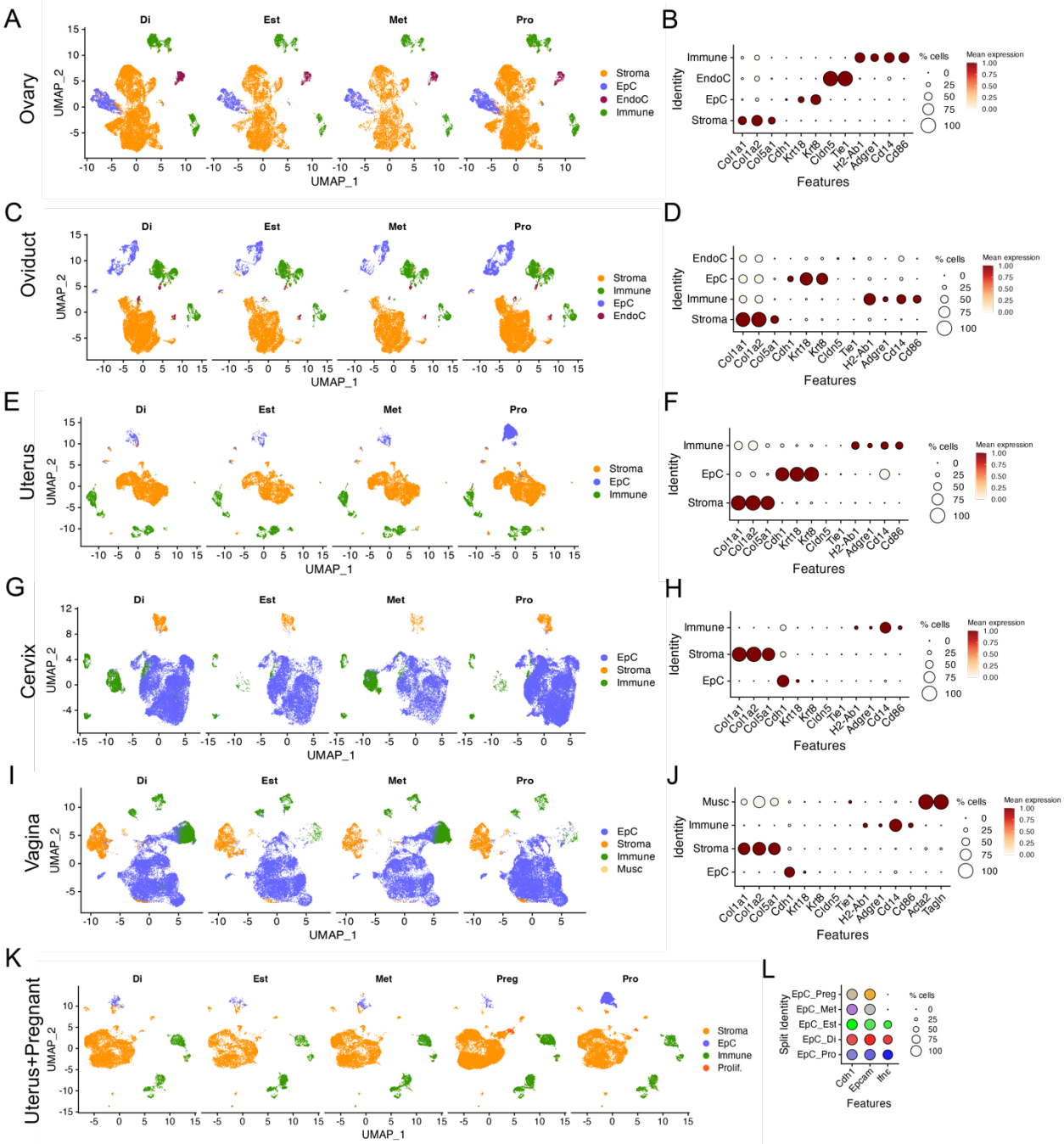

Supplemental Figure 2. (A, C, E, G, I) UMAPS showing clustering of stromal (Stroma, orange), epithelial (EpC, blue), immune (Immune, green), endothelial (EndoC, red), and muscular (Musc, yellow) cells within distinct phases of the estrous cycle the different tissues of the female reproductive tract (FRT) shown at left. **(D, F, H, J),** DotPlot of canonical markers in Oviduct (D), Uterus (F), Cervix (H), Vagina (J), and Uterus (J). **(K),** UMAP of uterine tissue throughout the estrous cycle and pregnant uterus (Preg). **(L),** DotPlot of cadherin-1 (*Cdh1*), *Epcam*, and *Ifnε* in uterine tissue split by phase of the estrous cycle or pregnancy (in orange).

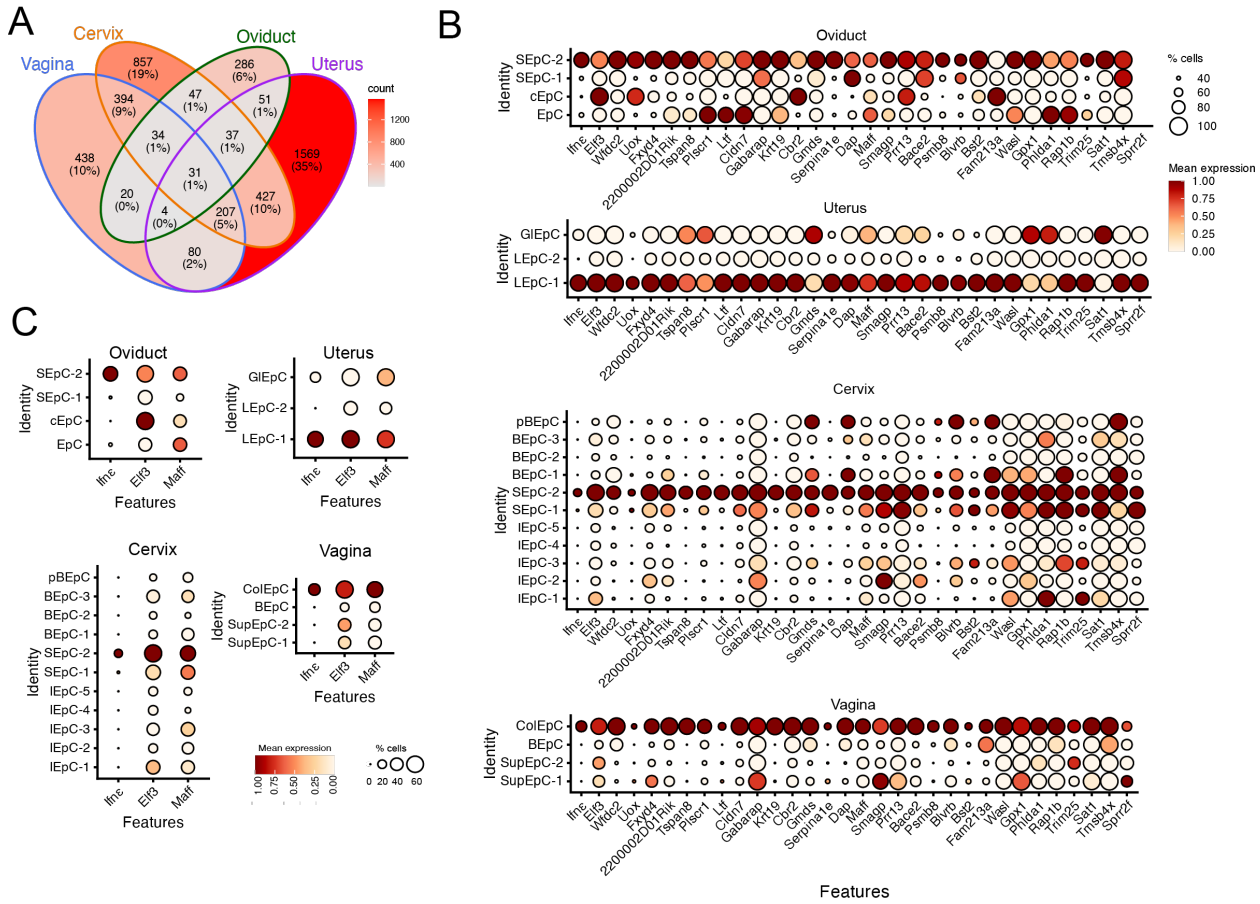

Supplemental Figure 3. (A), Venn diagram denoting the overlap of gene enriched in Ifnε-expressing clusters from Oviduct (green), Uterus (purple), Cervix (orange), and Vagina (blue). Key at right with red indicating the highest number of genes. The percent of overlap is also shown. **(B),** DotPlot of the genes differentially enriched in *Ifnε*-expressing clusters in Oviduct (top), Uterus (second from top), Cervix (second from bottom), and Vagina (bottom). Key and scale at right. **(C),** DotPlot of the expression of *Ifnε*, *Elf3*, and *Maff* in Oviduct, Uterus, Cervix, or Vagina as indicated. Key and scale at bottom.

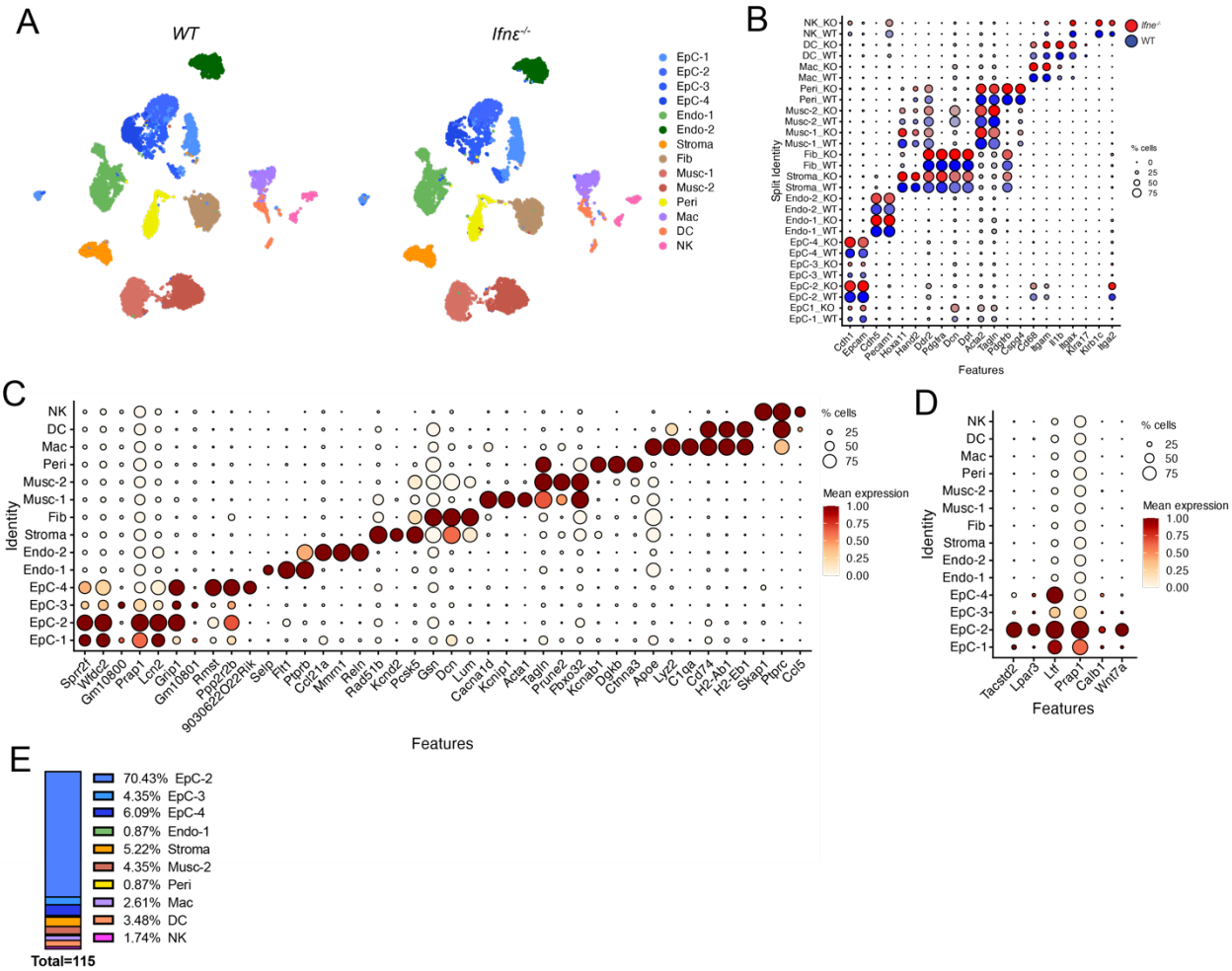

Supplemental Figure 4. (A), UMAP of cell clusters in uterine tissue isolated from WT (left) of Ifnε$^{-/-}$ mice (right) split by genotype. (B), DotPlot of canonical cell markers in WT (blue) or *Ifnε*$^{-/-}$ (red) mice. **(C),** DotPlort of cell type markers in the combined dataset from WT and *Ifnε*$^{-/-}$ mice. Scale and key at right. (D), DotPlot of luminal cell markers in WT and *Ifnε*$^{-/-}$ dataset. Key and scale at right. (E), Bar plot indicating the cell clusters associated with differentially upregulated genes (115 total) in WT mice compared to *Ifnε*$^{-/-}$ mice. The percent is shown at right.

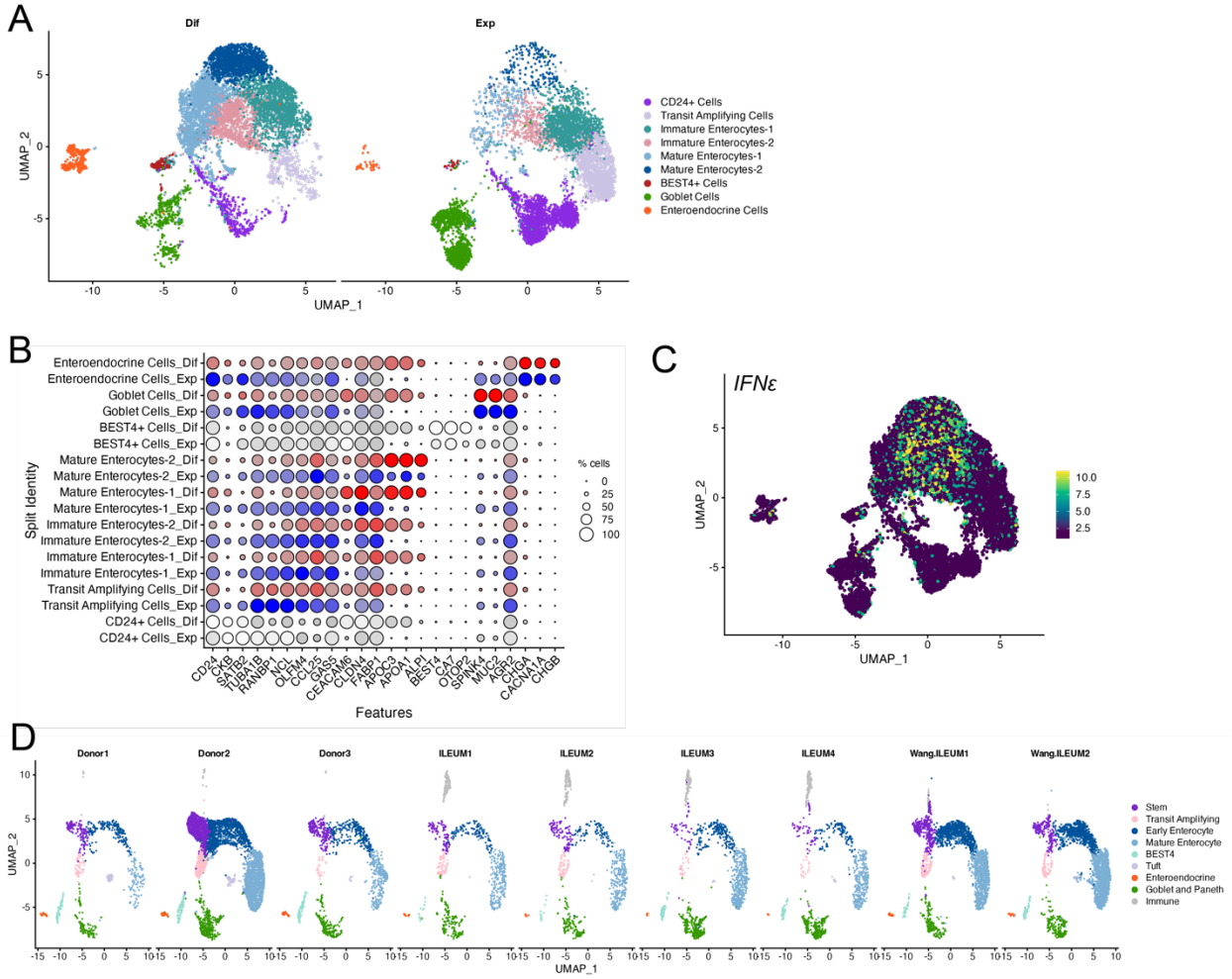

Supplemental Figure 5. (A), UMAP of cell clusters in enteroids cultured under expansion (Exp) or differentiated (Dif) conditions. **(B),** DotPlot of canonical makers in enteroids split by either Dif (red) or Exp (blue) growth conditions. **(C),** FeaturePlot of *IFNE* in enteroids. Scale at right. **(D)**, UMAP of human intestine dataset split by original sample.

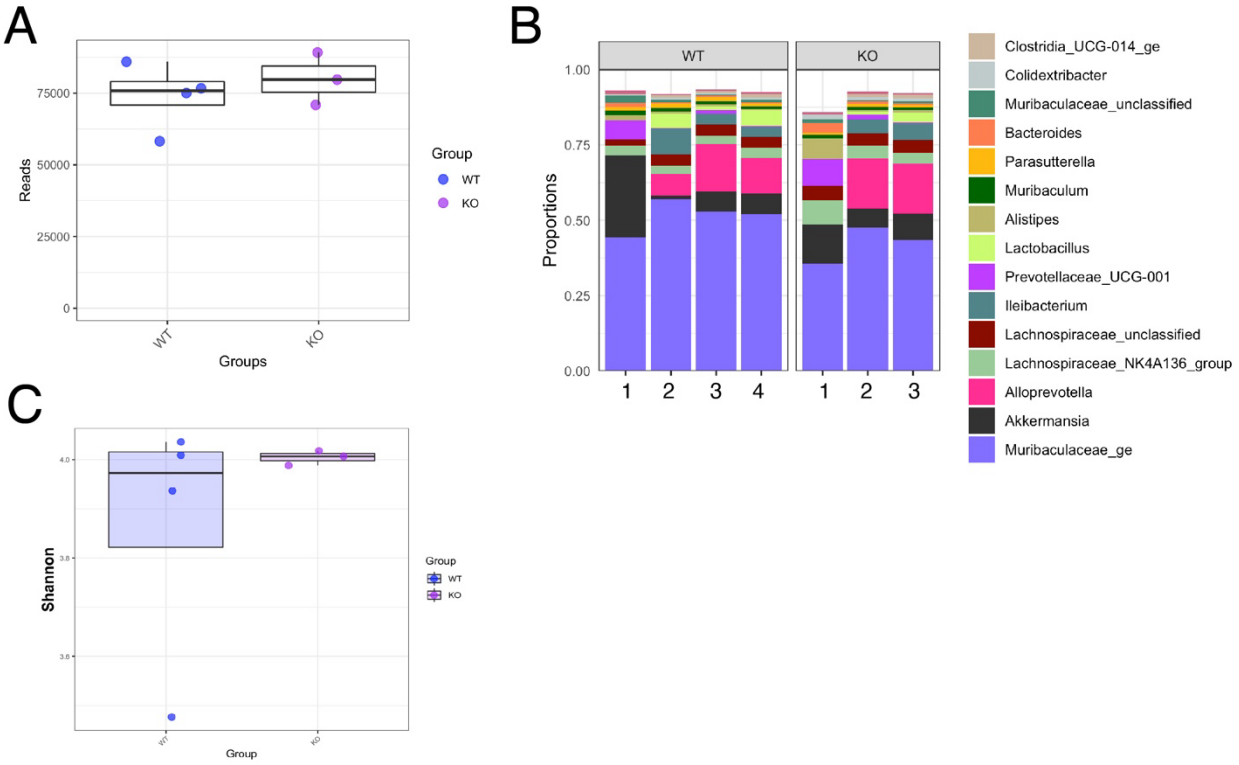

Supplemental Figure 6. (A), Total reads generated from 16S sequencing on fecal samples from *Ifn*$^{+/-}$ (WT) and *Ifnε*$^{-/-}$ (KO) littermates **(B),** Proportions of OTUs at each taxonomic rank in each sample **(C)** Alpha diversity measured by Shannon Index for *Ifnε*$^{+/-}$ (WT) and *Ifnε*$^{-/-}$ (KO) littermates.

Literature Cited

Beumer, J., J. Puschhof, F.Y. Yengej, L. Zhao, A. Martinez-Silgado, M. Blotenburg, H. Begthel, C. Boot, A. van Oudenaarden, Y.G. Chen, and H. Clevers. 2022. BMP gradient along the intestinal villus axis controls zonated enterocyte and goblet cell states. *Cell Rep* 38:110438.

Bourke, N.M., S.L. Achilles, S.U. Huang, H.E. Cumming, S.S. Lim, I. Papageorgiou, L.J. Gearing, R. Chapman, S. Thakore, N.E. Mangan, S. Mesiano, and P.J. Hertzog. 2022. Spatiotemporal regulation of human IFN-epsilon and innate immunity in the female reproductive tract. *JCI Insight* 7:

Burclaff, J., R.J. Bliton, K.A. Breau, M.T. Ok, I. Gomez-Martinez, J.S. Ranek, A.P. Bhatt, J.E. Purvis, J.T. Woosley, and S.T. Magness. 2022. A Proximal-to-Distal Survey of Healthy Adult Human Small Intestine and Colon Epithelium by Single-Cell Transcriptomics. *Cell Mol Gastroenterol Hepatol* 13:1554-1589.

Byers, S.L., M.V. Wiles, S.L. Dunn, and R.A. Taft. 2012. Mouse estrous cycle identification tool and images. *PLoS One* 7:e35538.

Coldbeck-Shackley, R.C., O. Romeo, S. Rosli, L.J. Gearing, J.A. Gould, S.S. Lim, K.H. Van der Hoek, N.S. Eyre, B. Shue, S.A. Robertson, S.M. Best, M.D. Tate, P.J. Hertzog, and M.R. Beard. 2023. Constitutive expression and distinct properties of IFN-epsilon protect the female reproductive tract from Zika virus infection. *PLoS Pathog* 19:e1010843.

de Geus, E.D., J.S. Volaric, A.Y. Matthews, N.E. Mangan, J. Chang, J.D. Ooi, N.A. de Weerd, E.M. Giles, and P.J. Hertzog. 2024. Epithelially Restricted Interferon Epsilon Protects Against Colitis. *Cell Mol Gastroenterol Hepatol* 17:267-278.

Demers, A., G. Kang, F. Ma, W. Lu, Z. Yuan, Y. Li, M. Lewis, E.N. Kraiselburd, L. Montaner, and Q. Li. 2014. The mucosal expression pattern of interferon-epsilon in rhesus macaques. *J Leukoc Biol* 96:1101-1107.

Fujii, M., M. Matano, K. Toshimitsu, A. Takano, Y. Mikami, S. Nishikori, S. Sugimoto, and T. Sato. 2018. Human Intestinal Organoids Maintain Self-Renewal Capacity and Cellular Diversity in Niche-Inspired Culture Condition. *Cell Stem Cell* 23:787-793 e786.

Fung, K.Y., E.D. de Geus, L. Ying, H. Cumming, N. Bourke, S.C. Foster, and P.J. Hertzog. 2024. Expression of Interferon Epsilon in Mucosal Epithelium is Regulated by Elf3. *Mol Cell Biol* 44:334-343.

Fung, K.Y., N.E. Mangan, H. Cumming, J.C. Horvat, J.R. Mayall, S.A. Stifter, N. De Weerd, L.C. Roisman, J. Rossjohn, S.A. Robertson, J.E. Schjenken, B. Parker, C.E. Gargett, H.P. Nguyen, D.J. Carr, P.M. Hansbro, and P.J. Hertzog. 2013. Interferon-epsilon protects the female reproductive tract from viral and bacterial infection. *Science* 339:1088-1092.

Garcia-Minambres, A., S.G. Eid, N.E. Mangan, C. Pade, S.S. Lim, A.Y. Matthews, N.A. de Weerd, P.J. Hertzog, and J. Mak. 2017. Interferon epsilon promotes HIV restriction at multiple steps of viral replication. *Immunol Cell Biol* 95:478-483.

Hafemeister, C., and R. Satija. 2019. Normalization and variance stabilization of single-cell RNA-seq data using regularized negative binomial regression. *Genome Biol* 20:296.

Hardy, M.P., C.M. Owczarek, L.S. Jermiin, M. Ejdeback, and P.J. Hertzog. 2004. Characterization of the type I interferon locus and identification of novel genes. *Genomics* 84:331-345.

He, G.W., L. Lin, J. DeMartino, X. Zheng, N. Staliarova, T. Dayton, H. Begthel, W.J. van de Wetering, E. Bodewes, J. van Zon, S. Tans, C. Lopez-Iglesias, P.J. Peters, W. Wu, D. Kotlarz, C. Klein, T. Margaritis, F. Holstege, and H. Clevers. 2022. Optimized human intestinal organoid model reveals interleukin-22-dependency of paneth cell formation. *Cell Stem Cell* 29:1333-1345 e1336.

Jin, S. 2019. Bipotent stem cells support the cyclical regeneration of endometrial epithelium of the murine uterus. *Proc Natl Acad Sci U S A* 116:6848-6857.

Korsunsky, I., N. Millard, J. Fan, K. Slowikowski, F. Zhang, K. Wei, Y. Baglaenko, M. Brenner, P.R. Loh, and S. Raychaudhuri. 2019. Fast, sensitive and accurate integration of single-cell data with Harmony. *Nat Methods* 16:1289-1296.

Kozich, J.J., S.L. Westcott, N.T. Baxter, S.K. Highlander, and P.D. Schloss. 2013. Development of a dual-index sequencing strategy and curation pipeline for analyzing amplicon sequence data on the MiSeq Illumina sequencing platform. *Appl Environ Microbiol* 79:5112-5120.

Love, M.I., W. Huber, and S. Anders. 2014. Moderated estimation of fold change and dispersion for RNA-seq data with DESeq2. *Genome Biol* 15:550.

Marks, Z.R.C., N. Campbell, N.A. deWeerd, S.S. Lim, L.J. Gearing, N.M. Bourke, and P.J. Hertzog. 2019. Properties and Functions of the Novel Type I Interferon Epsilon. *Semin Immunol* 43:101328.

Marks, Z.R.C., N.K. Campbell, N.E. Mangan, C.J. Vandenberg, L.J. Gearing, A.Y. Matthews, J.A. Gould, M.D. Tate, G. Wray-McCann, L. Ying, S. Rosli, N. Brockwell, B.S. Parker, S.S. Lim, M. Bilandzic, E.L. Christie, A.N. Stephens, E. de Geus, M.J. Wakefield, G.Y. Ho, O. McNally, S. Australian Ovarian Cancer, I.A. McNeish, D.D.L. Bowtell, N.A. de Weerd, C.L. Scott, N.M. Bourke, and P.J. Hertzog. 2023. Interferon-epsilon is a tumour suppressor and restricts ovarian cancer. *Nature* 620:1063-1070.

Matsumiya, T., S.M. Prescott, and D.M. Stafforini. 2007. IFN-epsilon mediates TNF-alpha-induced STAT1 phosphorylation and induction of retinoic acid-inducible gene-I in human cervical cancer cells. *J Immunol* 179:4542-4549.

Mayall, J.R., J.C. Horvat, N.E. Mangan, A. Chevalier, H. McCarthy, D. Hampsey, C. Donovan, A.C. Brown, A.Y. Matthews, N.A. de Weerd, E.D. de Geus, M.R. Starkey, R.Y. Kim, K. Daly, B.J. Goggins, S. Keely, S. Maltby, R. Baldwin, P.S. Foster, M.J. Boyle, P.S. Tanwar, N.D. Huntington, P.J. Hertzog, and P.M. Hansbro. 2024. Interferon-epsilon is a novel regulator of NK cell responses in the uterus. *EMBO Mol Med* 16:267-293.

Miller, D., R. Romero, M. Kacerovsky, I. Musilova, J. Galaz, V. Garcia-Flores, Y. Xu, E. Pusod, C. Demery-Poulos, P. Gutierrez-Contreras, T.N. Liu, E. Jung, K.R. Theis, L.A. Coleman, and N. Gomez-Lopez. 2022. Defining a role for Interferon Epsilon in normal and complicated pregnancies. *Heliyon* 8:e09952.

Nguyen, N.K., E.C. Deehan, Z. Zhang, M. Jin, N. Baskota, M.E. Perez-Munoz, J. Cole, Y.E. Tuncil, B. Seethaler, T. Wang, M. Laville, N.M. Delzenne, S.C. Bischoff, B.R. Hamaker, I. Martinez, D. Knights, J.A. Bakal, C.M. Prado, and J. Walter. 2020. Gut microbiota modulation with long-chain corn bran arabinoxylan in adults with overweight and obesity is linked to an individualized temporal increase in fecal propionate. *Microbiome* 8:118.

Ohtsuka, M., M. Sato, H. Miura, S. Takabayashi, M. Matsuyama, T. Koyano, N. Arifin, S. Nakamura, K. Wada, and C.B. Gurumurthy. 2018. i-GONAD: a robust method for in situ germline genome engineering using CRISPR nucleases. *Genome Biol* 19:25.

Pleguezuelos-Manzano, C., J. Puschhof, S. van den Brink, V. Geurts, J. Beumer, and H. Clevers. 2020. Establishment and Culture of Human Intestinal Organoids Derived from Adult Stem Cells. *Curr Protoc Immunol* 130:e106.

Robinson, C.M., M.A. Woods Acevedo, B.T. McCune, and J.K. Pfeiffer. 2019. Related Enteric Viruses Have Different Requirements for Host Microbiota in Mice. *J Virol* 93:

Satija, R., J.A. Farrell, D. Gennert, A.F. Schier, and A. Regev. 2015. Spatial reconstruction of single-cell gene expression data. *Nat Biotechnol* 33:495-502.

Schloss, P.D., S.L. Westcott, T. Ryabin, J.R. Hall, M. Hartmann, E.B. Hollister, R.A. Lesniewski, B.B. Oakley, D.H. Parks, C.J. Robinson, J.W. Sahl, B. Stres, G.G. Thallinger, D.J. Van Horn, and C.F. Weber. 2009. Introducing mothur: open-source, platform-independent, community-supported software for describing and comparing microbial communities. *Appl Environ Microbiol* 75:7537-7541.

Skavicus, S., and N.S. Heaton. 2023. Approaches for timeline reductions in pathogenesis studies using genetically modified mice. *Microbiol Spectr* 11:e0252123.

Stifter, S.A., A.Y. Matthews, N.E. Mangan, K.Y. Fung, A. Drew, M.D. Tate, T.P. Soares da Costa, D. Hampsey, J. Mayall, P.M. Hansbro, A. Garcia Minambres, S.G. Eid, J. Mak, J. Scoble, G. Lovrecz, N.A. deWeerd, and P.J. Hertzog. 2018. Defining the distinct, intrinsic properties of the novel type I interferon, IFNϵ. *J Biol Chem* 293:3168-3179.

Triana, S., M.L. Stanifer, C. Metz-Zumaran, M. Shahraz, M. Mukenhirn, C. Kee, C. Serger, R. Koschny, D. Ordonez-Rueda, M. Paulsen, V. Benes, S. Boulant, and T. Alexandrov. 2021. Single-cell transcriptomics reveals immune response of intestinal cell types to viral infection. *Mol Syst Biol* 17:e9833.

Wang, Y., W. Song, J. Wang, T. Wang, X. Xiong, Z. Qi, W. Fu, X. Yang, and Y.G. Chen. 2020. Single-cell transcriptome analysis reveals differential nutrient absorption functions in human intestine. *J Exp Med* 217:

Winkler, I., A. Tolkachov, F. Lammers, P. Lacour, K. Daugelaite, N. Schneider, M.L. Koch, J. Panten, F. Grunschlager, T. Poth, B.M. Avila, A. Schneider, S. Haas, D.T. Odom, and A. Goncalves. 2024. The cycling and aging mouse female reproductive tract at single-cell resolution. *Cell* 187:981-998 e925.

Zanin, N., C. Viaris de Lesegno, C. Lamaze, and C.M. Blouin. 2020. Interferon Receptor Trafficking and Signaling: Journey to the Cross Roads. *Front Immunol* 11:615603.